OPTIMIZATION OF COMMERCIALLY OFF THE SHELF (COTS) ELECTRIC PROPULSION SYSTEM FOR LOW SPEED FUEL CELL UAV

by

Muhammad Zulkifli

A Thesis Presented to the Faculty of the
American University of Sharjah
College of Engineering
in Partial Fulfillment
of the Requirements
for the Degree of

Master of Science in
Mechatronics Engineering

Sharjah, United Arab Emirates

March 2013

Approval Signatures

We, the undersigned, approve the Master's Thesis of Muhammad Zulkifli.

Thesis Title: Optimization of Commercially Off The Shelf (COTS) Electric Propulsion System for Low Speed Fuel Cell UAV

Signature **Date of Signature** *(dd/mm/yy)*

_____ _____

Dr. Mohammad Amin Al Jarrah
Professor, Department of Mechanical Engineering
Thesis Advisor

_____ _____

Dr. Aydin Yesildirek
Associate Professor, Department of Electrical Engineering
Thesis Committee Member

_____ _____

Dr. Mehmet Fatih Orhan
Assistant Professor, Department of Mechanical Engineering
Thesis Committee Member

_____ _____

Dr. Aydin Yesildirek
Director,
Mechatronics Graduate Program

_____ _____

Dr. Hany El Kadi
Associate Dean, College of Engineering

_____ _____

Dr. Hany El Kadi
Acting Dean, College of Engineering

_____ _____

Dr. Khaled Assaleh
Director of Graduate Studies

Acknowledgement

I would like to express my endless gratitude to Allah for always helping me in every situation during this work. Thank you also to Dr. Mohammad Al-Jarrah for his support and guidance in my thesis, and during my time as graduate student in AUS, and all of my colleagues that helped me directly and indirectly for this work. I would also like to thank the members and former members of the AUS aeronautics labs, Sonny Adiyansah, M. Angga Rachmansyah, John Mempin, Sheruzzaman Chowdurry, Kumar Saurav, Murad Qasimieh, and Ahmad Alshoubaki for the sharing of knowledge and experiences among us. I dedicated my thank you for colleague in AUS mechatronics program, Kamal Saeddedin, Waqqas Khan, Naveed Abbasi, Shivakummar, Hichem Zakaria Aichour, Adnan Sohail and Kent Roferos. Many thanks also to my colleagues M. Taha Khot for helping me in the CATIA drawing and also Emad Iqbal.

Finally, I would to thank my parents for always supporting me from the beginning until the finish of my masters program. Finally, a very special thank you goes to my fiancé, Yunita Fitra Andriana, for whom I dedicated my work. Thank you for everything; you are my inspiration to thrive in all my efforts, and you have been caring, reminding and challenging me to be better than ever. Be ready for our next journey together.

Abstract

Fuel cell technology offers higher energy density than any other onboard electric power source. However, despite its high energy content per unit mass, the fuel cell is lacking in power density ratio compared to Lithium-Polymer battery which is commonly used for UAV application. Therefore, the design of the unmanned aerial vehicle and its propulsion system must be properly sized and matched. This work addresses this problem through a design-optimization approach. The work focuses on optimizing the selection of the propulsion system components for one specific unmanned aerial vehicle designed in house. The main goal is to reach maximum endurance with the AEROPAK fuel cell system as the power source. Each component of the propulsion system is modeled based on a physical model except for the propeller which uses an artificial neural network. All the models are simultaneously solved with the “fsolve” function in Matlab to evaluate endurance and act as a fitness function for the genetic algorithm. The genetic algorithm is implemented on the outer loop of the optimization as to search the optimal solution according to the fitness function. The optimization process selects the propeller, motor, and the reduction gear ratio that will yield the best cruise endurance for a given unmanned aerial vehicle design. The components used in the optimization are commercially available. It is found out that the low Kv motor and large diameter propeller offer higher endurance since the current requirement to produce the same thrust is lower. The hydrogen consumption is dictated by the amount of current drawn from the fuel cell stack. Through this methodology, the exhaustive tradeoff between these elements can be avoided. The results are then validated against the wind tunnel test data. Results show more than a 13% endurance increase in all cases studied including maximum speed, maximum range, and maximum endurance.

Search Terms: genetic algorithm, fuel cell UAV, electric propulsion, design and optimization, multi-disciplinary analysis.

Table of Contents

List of Tables

List of Figures

Nomenclature

c	Mean aerodynamic chord	m
c_r	Wing chord at root	m
c_t	Wing chord at tip	m
c_b	Propeller blade local chord length	m
$\frac{dT}{dr}$	Thrust variation across propeller blade radius	-
$\frac{dQ}{dr}$	Torque variation across propeller blade radius	-
d_p	Propeller diameter	in
e	Oswald efficiency factor	-
f	Prandtl's tip loss factor	-
g	Earth gravity acceleration	$m.s^{-2}$
k_{blade}	Number of propeller blade	-
k_{loss}	Rate of the efficiency decreases as the duty cycle decreases	-
m_{total}	Total mass of the aircraft	kg
n	The amount of gas	moles
t/c	Thickness ratio of the airfoil	-
r	Radius	m
v	Relative airspeed	$m.s^{-1}$
AR	Aspect ratio	-
C_D	Coefficient of drag	-
$\widetilde{C_D}$	Coefficient of drag at the propeller blade section	-
$C_{D_{induce}}$	Induced drag coefficient	-
$C_{D_{parasitic}}$	Parasitic drag coefficient	-
C_L	Coefficient of lift	-
$\widetilde{C_L}$	Coefficient of lift at the propeller blade section	-
C_T	Coefficient of thrust	-

C_P	Coefficient of power	-
C_Q	Coefficient of torque	-
Cl_α	Changes of lift coefficient with angle of attack	$rads^{-1}$
Cl_0	Coefficient of lift at zero angle of attack	-
Cl_{max}	Maximum coefficient of lift	-
D	Drag force	N
D_c	Duty cycle	-
$\widetilde{D}$	Drag force at propeller blade section	N./unit length
E_m	Back EMF voltage	V
F	Faraday constant	$A.h.mol^{-1}$
$\widetilde{F_\theta}$	Circumferential force	N./unit length
G_r	Gear ratio	-
I_m	Motor current	A
I_0	No-load motor current	A
I_p	Propulsive current	A
I_{fc}	Fuel cell current	A
J	Advance ratio	-
K_b	Back EMF constant	Volts/RPM
K_t	Torque constant	N.m/A
K_v	Motor voltage constant	$RPM.v^{-1}$
M_{tip}	Propeller tip Mach number	-
$\dot{N_{H2}}$	Molar rate of the hydrogen gas	-
N_{cells}	Number of fuel cell voltage stack	-
P	Pressure	kPa
$P_{available}$	Power available	W
$P_{required}$	Power required	W
Q	Torque	N.m
Q_m	Motor torque	N.m

R	Ideal gas constant	-
R_{cont}	Controller resistance	Ohm
R_e	Reynolds number	-
S, S_{ref}	Wing reference area	m^2
T	Thrust force	N
$\tilde{T}$	Thrust force at propeller blade section	N./unit length
U_{H2}	Hydrogen utilization	-
V	Volume	m^3
V_0	No-load motor voltage	V
V_b	Resultant velocity relative to the cross – section	$m.s^{-1}$
V_i	Induced velocity	$m.s^{-1}$
V_{fc}	Fuel cell voltage	V
V_p	Propulsive voltage	V
V_∞	Forward relative velocity	$m.s^{-1}$
V_{xi}	Induced velocity component in x direction	$m.s^{-1}$
$V_{\theta i}$	Induced velocity component in θ direction	$m.s^{-1}$
V_{min}	Minimum cruising airspeed	$m.s^{-1}$
V_t	Terminal motor voltage	V
α_b	Propeller blade angle of attack	radians
α_{0}l	Zero lift angle of attack	radians
$\alpha_{L0}(r)$	Zero lift angle of attack of the blade airfoil section	radians
$\beta(r)$	Aerodynamics pitch angle (section 3.3), The motor drag coefficient (section 3.4)	radians
$\beta_c(r)$	Chord line pitch angle	radians
β_t	Aerodynamics pitch angle at propeller tip.	radians
$\varepsilon_\infty(r)$	Propeller blade section advance angle	radians
$\varepsilon_b(r)$	Propeller blade section downwash angle	radians
$\varepsilon_i(r)$	Propeller blade section induced angle	radians

μ	Fluid dynamic viscosity	-
ρ	Air density	$Kg.m^{-3}$
π	Mathematical constant (3.14159)	-
ω	Propeller rotational speed	$rad.s^{-1}$
ω_m	Motor rotational speed	$rad.s^{-1}$
κ	Goldstein's Kappa Factor	-
λ_w	Wing taper ratio	-
Γ	Dihedral angle (section 3.1), local circulation (section 3.3)	radians, -
$\eta_{propeller}$	Propeller efficiency	-
η_{cont}	Controller efficiency	-
η_{motor}	Motor efficiency	-
AoA	Angle of attack	degrees
COTS	Commercially off the shelf	-
FSO	Full scale output	-
GA	Genetic algorithm	-
UAV	Unmanned aerial vehicle	-

1. Introduction

1.1. Background

Nowadays, unmanned aerial vehicles are used for many applications. These range from simple aerial photography to complex military applications such as intelligence, surveillance, and reconnaissance missions. In general, UAV systems consist of the vehicle platform and an autonomous guidance and control system. Each application requires different design specifications of the vehicle platform and the autonomous guidance and control system. The vehicle platform consists of the airframe and the propulsion system. The autonomous system consists of the autopilot, navigation system, air data system, and a communication device between the ground station and the aircraft.

For surveillance purposes it is desired that a UAV system stay in the air as long as possible in order to keep monitoring the object of interest. The endurance of an aircraft is mainly related to the aerodynamic efficiency and the efficiency of the propulsion system that is used in the aircraft. Small size and short range UAVs such as hand-launched UAVs use an electric motor-driven propulsion system. The present work is addressing this class of UAVs.

In the past decade, fuel cell technology emerged as one of the alternative power sources of the UAV system. This is because fuel cells offer higher energy density compared with existing batteries. The energy density of an advanced battery can reach up to 200 Wh/kg at the module level, while the fuel cell can reach more than 800 Wh/kg at the system level [1]. The implication of this fact on the UAV system is that the endurance can be improved almost four times with the same weight when compared with available batteries. Several attempts of demonstrating the usability of fuel cell systems in UAVs were made by some UAV manufacturers as well as research institutes [2] as shown in Table 1 Fuel cell powered UAVs [2].

Maximizing the endurance of the aircraft cannot be solely based on the amount of fuel or increasing the capacity of the battery. Increasing fuel will increase the weight and the engine size will increase as well. Moreover, to achieve longer endurance, the amount of drag that the aircraft produces while flying determines the required thrust to maintain the flight. Thus, the designer should produce a well-optimized design of the UAV platform from a performance point of view. This can be achieved by applying an optimization routine in the design loop of the UAV. The

optimization approach should be applied to the aerodynamic and propulsion system analysis and synthesis. The selection of propulsion system components has a major contribution in influencing the endurance of the aircraft.

Table 1 Fuel cell powered UAVs [2]

Organization (date)	Fuel Cell Type	Reactant Storage Type	Endurance (est.)
AeroVironment (2003)	PEM	H2 Sodium Borohydride	0.2 hr
AeroVironment (2005)	PEM	H2 Cryogenic	24 hr
Naval Research Lab (2006)	PEM	H2 Gaseous	3.3 hr
Georgia Inst. of Tech. (2006)	PEM	H2 Gaseous	0.75 hr
CSU Los Angeles (2006)	PEM	H2 Gaseous	0.75 hr
CSULA/OSU (2007)	PEM	H2 Gaseous	12 hr
KAIST (2007)	PEM	H2 Sodium Borohydride	10 hr
Adaptive materials inc (2006)	SOFC	Propane	4 hr
AeroVironment (2007)	PEM	H2 Sodium Borohydride	9 hr
DLR/HyFish (2006)	PEM	H2 Gaseous	0.25 hr

Despite the fact that there are fuel cell powered UAV studies, the design methodology and optimization of a fuel cell powered UAV is still not mature. This work will focus on the propulsion system optimization part of fuel cell powered UAVs. Since a low cost yet optimized design solution is desired, the propulsion system components considered here are restricted to only the commercially off-the-shelf components available at the moment. Moreover, most of the electric propulsion system components that are available commercially off-the-shelf are not designed for fuel cell characteristic.

1.2. Literature Review

This section consists of a brief review of the work that has been done on aircraft design powered by fuel cell propulsion systems. Moffit in [3] approached the design solution from a conceptual point of view. The author used a design space exploration to characterize the aircraft configuration and the fuel cell sizing as one integrated system starting at the conceptual design level. The author proposed a design space exploration on a high level design task by using a grid search. The optimal design identified in the high-level conceptual design task is then used as the basis for the detailed design of the aircraft components. However, the approach is very extensive and exhaustive due to exploration of design space that has very broad dimension and length require high computational cost. It is impractical to be use as a

design tool. Despite high computational cost of the method, the author found that matching the motor and propeller to the characteristics of a given fuel cell is the most important aspect of a successful design.

Ofuma in [4] presented the development of a hydrogen fuel cell powered UAV. The author used computer-aided engineering software to help verify the design performance. The author suggests using a high aspect ratio wing as it is able to efficiently utilize the low power-to-weight ratio of the fuel cell power plant that was used. However, the design approach used was conventional without optimization routine. Therefore, the result is not guaranteed to result in an optimal solution.

Lindahl, in [5] presented a design approach, simulation and validation of a UAV propulsion system powered by an SOFC fuel cell. The system components' models were physical-based models at a steady state condition. The implication of different selection of propulsion system components to the performance was explored. This study, however, only addressed the connection between fuel cell polarization curve and the ability of fuel cell to command thrust.

In [6] the author suggested that the hybridization of the fuel cell with a battery would give the UAV higher power, for a short time, compared with the power produced by the fuel cell only. This method would address the fuel cell low power density problem while maintaining a light weight fuel cell system. The propulsion system selection process was done through trial and error. The author picked some set up specifications of propulsion system components that had been through calculation. Then the author preformed some dyno – tests in static and wind tunnel environments to evaluate the performance. However, the evaluation process of the propulsion system components through a dyno – test is only useful when the selection of each component is finalized. His methodology in selection of the components cannot guarantee the optimal solution.

The energy management strategy in hybrid fuel cell propulsion systems is investigated in [7]. The author found that if the fuel cell were able to meet all possible power required by the motor and propeller pair, the hybrid battery system would not improve the endurance. Hybrid systems allow decoupling of the aircraft power design requirement for climb and cruise. The integrated design process is able to take advantage of this decoupling which can improve the performance of hybrid fuels cell over conventional powered aircrafts.

Recently, [8] presented the conceptual design, development, and flight tests performed for an extended endurance fuel cell (FC) powered unmanned aircraft. The HiLS result was promising for the fuel cell UAV to achieve 24 hour endurance. The UAV that flies using autopilot during the cruise consumes power 60% less than the piloted (RC controlled) flight. The utilization of an autopilot system might improve the endurance of the UAV as well.

The design method to develop a hand launch UAV for long endurance operation was developed by utilizing multi-disciplinary design tools coupled with an optimization routine [9]. It used a genetic algorithm as its optimization routine due to the capability to find many near-optimal designs, providing many options when selecting a final design configuration. However, in this one it incorporated hand launch analysis and used a battery as the power source instead of a fuel cell.

Therefore in this thesis, the work focuses on matching the propeller, gear ratio and motor to the fuel cell characteristics and proposes a solution which offers the best endurance. Since it is not practical to find the optimal solution by exploring the entire design space, all possible design proposals are explored in order to find the optimal solution using an optimization routine. Some of the propulsion system components are selected from commercially available off-the-shelf components. The optimization process involves variables that are discrete and continuous as well. Therefore, the genetic algorithm (GA) is used in this work due to its ability to handle mixed discrete continuous optimization problems and because of being modular regardless of the application [10].

The GA is used in selecting the specification of propulsion system components from COTS with the goal of having the best endurance for the propulsion system airframe combination. In conjunction with GA, an analysis tool is developed in order to evaluate the system performance of the entire propulsion system and the UAV platform. The UAV platform flight performance is the function of many aspects such as aerodynamics, propulsion, control and structure. Thus, by nature this problem is involving several engineering disciplines. Therefore the analysis tool is called multi-disciplinary analysis. This tool is developed to evaluate the interaction between each subsystem to determine the flight performance of UAV, (i.e., endurance and range). However, the control discipline is not considered here since the interest here is to get maximum endurance where the flight mostly performed at steady level condition.

If the design of the UAV platform is fixed then the optimization will not address finding the optimal UAV configuration that yields the optimum flight performance. Thus, the aerodynamic characteristic is determined and not included as a design variable. Moreover, the fuel cell system is also fixed not included as a design variable since the fuel cell system is already available and particularly designed for aeronautics application. It is called Aeropak™ and is capable of delivering 200 watts of power continuously. It has a hydrogen storage system in a compressed gas cylinder with 1.1L and up to 150 bars.

1.3. Thesis Objectives

This thesis aims to develop a design optimization tool for a UAV with an electric propulsion system powered by a fuel cell. The optimization tool is intended to be used for the selection of the electronic propulsion components to generate a thrust force for propelling the UAV. The objective in the optimization is to achieve the best endurance of continuous flight with electric power provided by the fuel cell system. The components should be selected from the existing components that are commercially available off the shelf from the market. Therefore, to achieve the development of this design optimization tool, there are four issues addressed in this thesis:

- Development of propulsion system models to be used in optimization process.
- Development of multi-disciplinary analysis for the propulsion system.
- Determination and implementation of the optimization method consistent with the design problem and constraints.
- Validation of the optimization tool results experimentally with a flight-simulated environment using a wind tunnel.

1.4. Contribution

This research will contribute to the literature in several ways including

1. Implementing a genetic algorithm for optimization of a propulsion system powered by a fuel cell.
2. Contributing to the American University of Sharjah by:
    - Developing and implementing a high-level multidisciplinary design and optimization tool for UAV platform integrated with the fuel cell block.

- Developing a propeller model based on electric APC propeller data provided by the manufacturer using an artificial neural network.
- Building an experimental test setup for propulsion system testing with variable wind speeds of 0 to 20 m/s.

1.5. Thesis Outline

This work is organized into 5 chapters as follows:

- Chapter 1 is an introduction about this work. This section describes the motivation behind the thesis topic and the expected outcomes from this work. This chapter also includes a literature review of some published materials about similar topics in the field.
- Chapter 2 describes the basic concepts and the theoretical background in aircraft design and electric propulsion systems. This chapter aims at giving a basic understanding of the topics to help formulate the problem of this thesis.
- Chapter 3 describes the system modeling used in the multi-disciplinary analysis and introduces the optimization theory implemented in this thesis. The multidisciplinary analysis estimates the electric fuel cell propulsion system performance based on the model. Taking design variables as an input set, the outcome is evaluated according to the optimization scheme.
- Chapter 4 presents the results obtained from the optimization and the wind tunnel test of the propulsion system.
- Chapter 5 presents the conclusions and proposed future work.

2. Basic Concepts

2.1. Introduction

This chapter explains the conceptual terms used in the work. The basic theory behind the mechanics of flight and fuel cell systems are described in this section. The technical reasoning behind the design loop used in the optimization is based on the theory explained here and in the next chapter.

When an airplane is flying there are aerodynamics, body and thrust forces acting on it. Thrust is the force that propels the airplane to move forward in its longitudinal axis. Lift is the aerodynamic force generated due to the airflow movement relative to the lifting surfaces component and perpendicular to the relative wind velocity. This force is used to compensate the weight force due to gravity. The drag force is the resistance force generated due to the friction and pressure drop when the airplane is moving relative to the air and is directed along the relative wind velocity. Figure 1 illustrates the forces acting on an airplane.

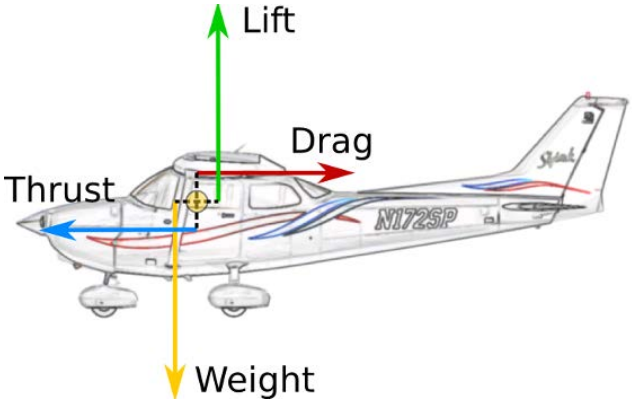

Figure 1 Forces Acting on Airplane [11]

The endurance of an aircraft is a function of many factors, aerodynamics efficiency, aircraft weight, fuel or energy consumption, etc. For the internal combustion engine, the duration of operating time is a factor of how much fuel can be stored in the fuel tank. Similarly, in electric propulsion systems the endurance depends on how much energy can be stored in the energy storage system such as a battery. However, the battery has a drawback in energy density as mentioned in the previous chapter. The fuel cell system offers almost four times the energy density of a typical battery [1]. It is thus a promising solution to use fuel cells to improve the endurance of electro propulsive driven unmanned aerial vehicles.

The fuel cell is used as a power provider for electric motors that drives the propeller to generate thrust force. The overall propulsion system is described in Figure 2. The fuel cell system consists of a fuel cell stack with an on board controller acting as a power management system. It has also a support battery that will help provide additional power when the load demands are higher than rated power of the fuel cell stack for a short period of time.

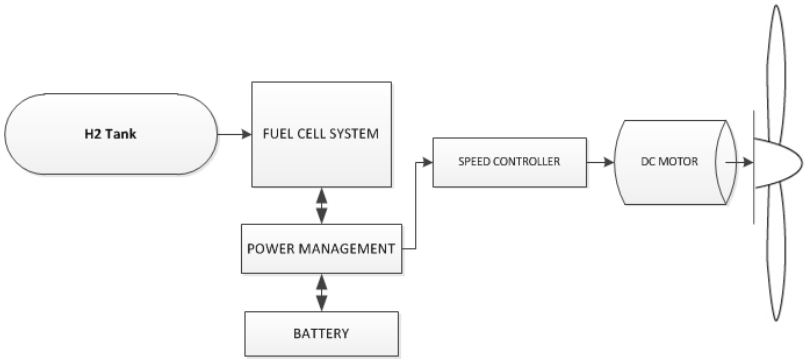

Figure 2 Propulsion System Overview

2.2. Aerodynamics

The aerodynamics forces are generated due to the circulation of airflow around the airfoil, creating a pressure difference distribution between the upper and lower surface. The total difference of pressure when integrated along the wing area can be represented as lift and drag. Figure 3 portrays a wing cross section in a laminar airflow.

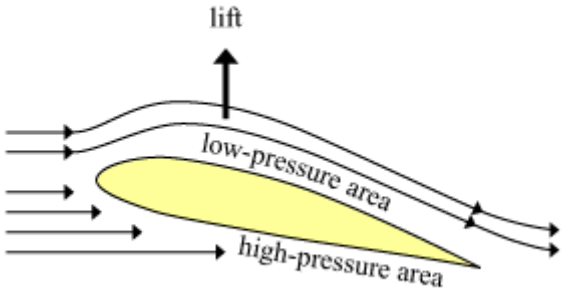

Figure 3 Wing cross section [12]

The lift and drag force are calculated using the following equations:

$$L = \frac{1}{2}\rho v^2 S C_L \quad \textbf{(1)}$$

$$D = \frac{1}{2}\rho v^2 S C_D \quad \textbf{(2)}$$

The ρ is air density, v is relative airspeed, and S is area of the lifting surface. C_L and C_D stand for coefficient of lift and coefficient of drag for the 3 dimensional wing. For airfoil the coefficients are written as $C_l$and C_d. Those two constants are a function of r that turns the propeller to generate thrust force. The overall propulsion system can is described in geometry of the airfoil, angle of attack and Reynolds number, Re. Reynolds number is a non-dimensional ratio that gives a measure of inertial force of the fluid and the viscosity of the fluid. The Reynolds number is defined in the following equation

$$R_e = \frac{\rho v c}{\mu} \quad \textbf{(3)}$$

where c is the chord length of the airfoil and μ is the fluid kinematic viscosity. In this regard, the fluid is the air. Figure 4 shows the relationship between the C_L and C_D value that change with the angle of attack. The C_L value increases along with the positive increment of angle of attack until it reaches the stalling point. At this point the maximum C_L value is reached. If the angle of attack is increased further the flow over the upper surface of airfoil starts to get separated and significant pressure loss occurs. Thus, the C_L value starts dropping and the wing loses lift force while drag increases significantly. Moreover, after this point the drag still continues to increase but without an increase in lift. As depicted in Figure 4 the C_d value also changes with the angle of attack and for every value of C_l there is a corresponding C_d value. This graph is unique for each airfoil and depends on the Reynolds number. The graph is generated from the XFLR5 program which simulates the airflow around Clark Y airfoil at Re 100,000.

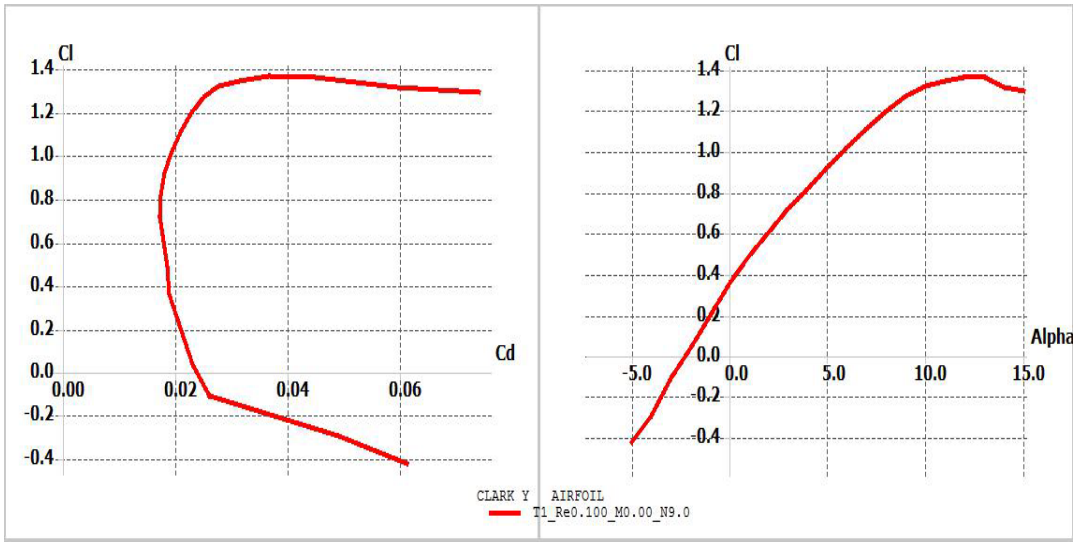

Figure 4 Drag Polar and Coefficient Lift Curve

In an actual wing the drag can be broken down into two components: parasitic drag and induced drag. Parasitic drag is the drag produced from non lifting parts such as fuselage and landing gears. The induced drag is drag produced due to the generation of lift. Equation (4) defines induced drag:

$$C_{D_{induce}} = \frac{C_L}{e\pi AR} \quad (4)$$

where AR is the aspect ratio of the wing. It is the ratio between wingspan suqaure and the wing planform area, and can be expressed as $AR = \frac{b^2}{S}$. The Oswald efficiency factor, e, is a factor that describes how close the lift is to the elliptical load distribution. The value is between 0 to 1, where 1 means the wing is elliptic. However, in most cases the Oswald efficiency factor, e, is between 0.75 to 0.85. In the end the total drag is the summation of each drag component as follows:

$$C_D = C_{D_{parasitic}} + C_{D_{induce}} \quad (5)$$

2.3. Propulsion System

The electronic propulsion system's basic components consist of a battery, a DC motor, a speed controller, and a propeller. This section explains the basic models of each part of the electronic propulsion system.

A battery is an energy storage device made of electrochemical materials. This device is able to convert chemically stored energy to an electrical charge when discharging. Batteries are composed of a metallic cathode and anode with an electrolyte substance in contact with them. There are several types of battery including lithium-ion and lithium-ion polymer, lead acid, nickel-cadmium (NiCd), nickel-metal-hydride (NiMH). The lithium-ion-polymer (LiPo) has the best energy density among them all. Due to this fact this kind of battery is commonly used in aerospace application. The voltage rating for one cell of this kind of battery is 3.7 V and its capacity depends on the size of the battery.

Batteries have a typical I-V polarization curve which describes the relation between the open circuit voltages and the current hour. The open circuit voltage is at the maximum when the battery is fully charged, and it drops as the energy is being consumed. Therefore, the voltage drop indicates the drop in energy contained in the battery. Figure 5 shows the discharge curve of the battery; this figure illustrates what has been explained earlier.

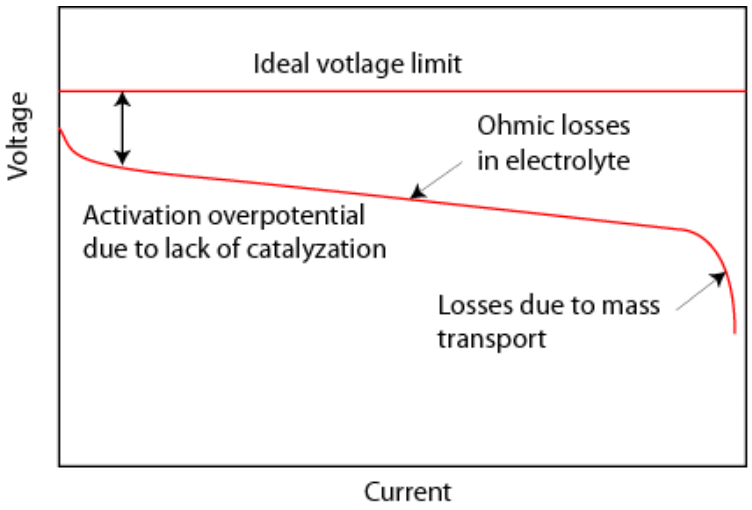

Figure 5 Battery Polarization I-V Curve [13]

2.4. Electric Motor

The electric motor discussed in this section is limited to direct current (DC). The two common types of DC electric motor are brushed and brushless. Both use commutation to create a rotating magnetic field vector that interacts with the permanent magnet or electromagnet. The commutation can be done either mechanically or by electronic commutation.

In general, an electric motor consists of a rotor, stator, coil, and permanent magnet or electromagnet. The rotor is the part that rotates when the electric motor is operating. The stator is the part that remains stationary. The configurations of how the magnetic field is generated between the coil and permanent magnet are many. The coil can be mounted on the rotor and the electrical connection can be ensured using brushes that have mechanical contact with the coil mounted on the rotor. The rotation will continuously change the coil polarity, yielding in an oscillating current. This configuration is called “brushed DC motor.” The brushed configuration creates sparks, friction and noise; all of these things create limitations, especially when the speed and current demands are higher.

For the brushless DC motor configuration, the coil is placed on the stator and the permanent magnet on the rotor. In order to get the same power distribution like the on the brushed motor, the commutation is performed by an electronic drive. The advantages of this configuration are many, including less noise, higher efficiency, longer lifetime, high reliability, precise speed control and cooler temperature compared to the brushed one.

2.5. Propeller

The propeller is a device that consists of two or more twisted plates that have an airfoil-shaped cross section in radial direction. Mounted to a rotating shaft in order to provide the propulsive force for the vehicle. When a propeller rotates inside the fluid, some amount of the fluid adjacent on the upstream of the propeller passes through. This happens due to the profile of the propeller blades built from sets of airfoil sections in radial direction. The acceleration of the incoming fluid particles creates a reaction force in the opposite direction of fluid flow.

The blade element theory approximates the propeller as a lifting surface and analyzes it as a lifting line. The lifting surface consists of a finite number of airfoil sections around which the pitch angle, chord, and airfoil section are distributed. Each section generates lift when the propeller blade is rotating with an angular velocity ω while advancing forward with relative velocity V_{∞}. Figure 6 describes the relation of angular velocity and advance velocity and the forces generated for each section. The total lift and drag generated are calculated and integrated along the blade. The thrust force generated from the propeller is heavily influenced by the propeller axial speed and the rotational speed of the propeller. When the propeller rotates there is resisting torque resulting from the lift and drag force components in rotational direction. The propeller efficiency varies with the axial speed and rotational speed; specifically it is called advance ratio (J). This is a ratio that describes the dimensionless measure of propeller axial speed to the rotational speed.

2.6. Fuel Cell

The fuel cell is an electrochemical device in the form of a cell that converts a source fuel into electrical current. The conversion of the fuel energy is an electrochemical process with water and heat as its by-product. The reaction between fuel and oxidant inside a cell triggered by an electrolyte generates electricity. It consumes the reactant from an external source, which are hydrogen and oxygen. As illustrated in Figure 7, the fuel cell offers many benefits in energy generation technology. The energy conversion process is clean, quiet, and efficient. The emission level of this fuel cell can reach up to zero if using hydrogen as the fuel. In addition, the fuel cells operate with low noise, which help to reduce the noise pollution.

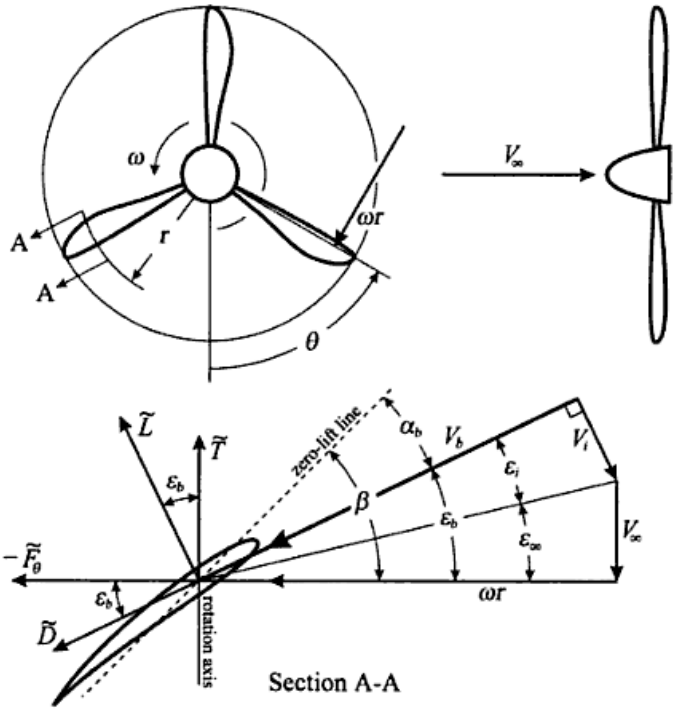

Figure 6 Propeller Aerodynamics Diagram [14]

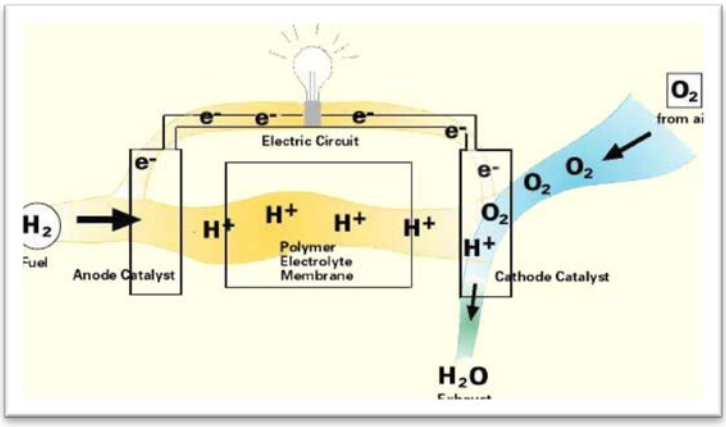

Figure 7 Illustration of Electrochemical Process in The Fuel Cell [15]

.

3. Modeling and Optimization

In this section modeling of each component of the UAV system are described. The models are used in the analysis of the calculated performance of the propulsion system. The goal of this process is to be able to evaluate the performance of the vehicle when the selected propulsion system specification is used in operation of the UAV. The performance of the UAV highlighted here is the endurance or the operating time of the UAV. Therefore, the models that are in the optimization are assumed steady state models due to the fact that dynamic response of the individual components is assumed to be fast compared to the flight time of the vehicle. This analysis is integrated inside the optimization scheme which is explained in the last section.

The optimization is limited to the given aircraft design. Therefore, the variables of airframe design and the aerodynamic model of the aircraft, are excluded from the design space. Thus, in the subsequent section the proposed aircraft design used in the analysis is introduced.

3.1. Proposed Aircraft Design

The fuel cell is well known for its high energy-to-weight density which results in higher storage of power with lower mass compared to other batteries. Since the mass of an aircraft fundamentally influences its flight performance, the lower the aircraft mass the lower the power required to maintain the flight of the aircraft. Hence, the fuel cell has good potential to be used as a power source for UAV, especially for long endurance operations.

Horizon Energy System has developed a fuel cell package for UAV application. The package is called AEROPAK™. It can provide 200 watts of power continuously and is incorporated with the hybrid Lithium Polymer battery that can provide 600 watts of power for short durations. Thus, the aircraft design should be suitable to this particular type of fuel cell, especially the power requirement. Therefore the design requirements of this aircraft are as follows:

- The maximum takeoff weight of the aircraft should be between 7 – 8 kg
- The maximum operational cruising speed is up to 19 m/s
- Power required for cruise should be less than 200 watts
- Cruising altitude should be at 1000 – 2000 m

A feasibility study was conducted in order to investigate the possibility of implementation of a 200W fuel cell on the UAV. The study involved calculation of some main parameters in aircraft design and compares it with data from the existing aircraft or UAV. To start the calculation, an initial guess was made of the wing area and aircraft weight. The weight of the aircraft is estimated by measuring the weight of the existing components such as the fuel cell, servos, hydrogen tank, battery, speed controller, propeller, and receiver. However, for the airframe, the weight is estimated by proportional factoring to the weight of the already-made composite wing (Vladimir Supra Pro - a commercially acquired composite wing). Table 2 shows the mass break down of the aircraft.

Table 2 UAV Mass Break Down

Parts	Weight	
Fuselage	1700	grams
Empennage	144	grams
ESC	100	grams
Wing	1100	grams
Fuel Cell	1800	grams
Autopilot	200	grams
Battery	500	grams
Receiver	80	grams
Landing Gear	500	grams
Servos	200	grams
Total	6324	grams
	6.324	Kilograms

The initial guess of the total weight of aircraft is 6.3 Kg without the motor and the propeller. According to this total weight, plus the approximate mass of the motor and propeller of 700 grams, the aircraft's minimum cruising speed is calculated against the coefficient of lift (C_L) by assuming that the wing area is 0.9 m^2. This calculation also considers that the plane flies at an altitude of 1000 m with the air density (ρ) being 1.2133 Kg/m^3 and gravity 9.81 m/s^2. Table 3 shows the variation of minimum cruising speed with respect to C_L.

As can be seen in Table 3 where C_L = 0.4, the minimum cruising speed is 17.7 m/s, which is the close to the requirement of maximum cruising speed. On the other hand, the lower cruise speed is possible for a certain wing area. However, it will require a higher aircraft coefficient of lift (C_L), which is difficult to achieve and less

practical. Thus, C_L = 0.4 is chosen as the design coefficient of lift. At this stage the airfoil type used is not determined yet and the aerodynamic performance of the aircraft is still unknown.

Table 3 Design C_L Variation Due to Velocity at Steady Level Flight

Cruise Condition L = W 68.7 N	
CL	V [m/s]
0.2	25.08
0.3	20.478
0.4	17.734
0.5	15.862
0.6	14.48
0.7	13.406
0.8	12.54
1	11.216
1.2	10.239

Since the power availability is only 200W, the drag of the aircraft is an important factor for achieving the objectives. The power required for the cruising flight should be less than 200W, where the relation of drag with power required during the flight is given by equation (6).

$$P_{req} = DV = 0.5\,\rho\,V^3 S_{ref} C_D \quad \textbf{(6)}$$

From this equation, the maximum coefficient of drag, C_D, for the aircraft can be determined from the relation between the power available and power required as shown in the Table 4. So the designed aircraft coefficient of drag should not exceed this value if it wants to use the Aeropak™ fuel cell at its rated output.

Table 4 Maximum Drag Coefficient

Max Power available	200 watts
C_D max	0.068709

However, in this section the details of the design process are beyond the scope of this work. Therefore, this thesis provides a summary of the proposed aircraft design to be used in the present study. The summary is presented in appendix A. The geometry of the proposed aircraft design is depicted in Figure 8, in units of millimeters. The configuration is a conventional airplane type.

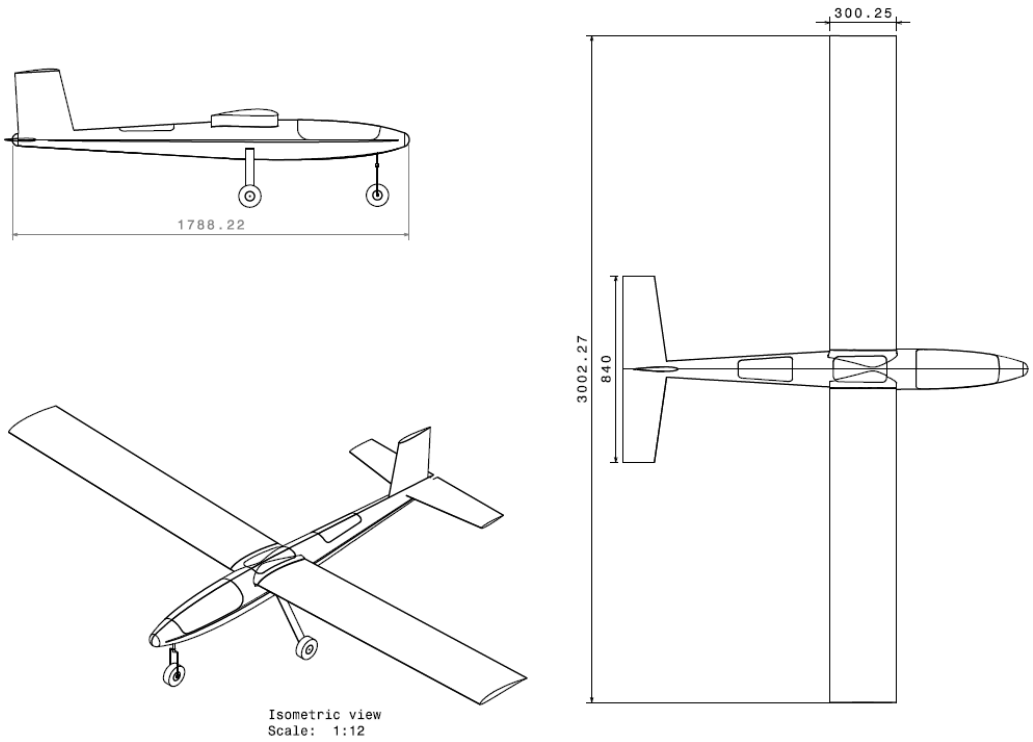

Figure 8 Tree View Drawing of Fuel Cell UAV

The wing geometry design specification is summarized in Table 5. The aircraft is designed in such away to have high aerodynamic efficiency, low drag, ease of manufacturing and low pitching moment. Thus, the wing airfoil selection is important and from a close study of several airfoil candidates, the SD7032 was selected as the wing airfoil. The aspect ratio of the wing is 10 and considered to be moderate. This choice was made due in order to compromise between difficulties in the manufacturing process and low drag wing. The aspect ratio determines the induced drag produced while the wing is moving through the air. The increases of aspect ratio of yields lower induced drag. The relationship between aspect ratio of the wing and induced drag is shown in equation (4).

Table 5 Wing Geometry Specification

Wing Geometry			
Wing Loading	W/S	7.5	Kg/m^2
Wing Area	S_{ref}	0.9	m^2
Wing Span	b_w	3	m
Aspect Ratio	AR_w	10	
Taper Ratio	λ_w	1	
Root Chord	c_r	0.3	m
Tip Chord	c_t	0.3	m
Mean Aerodynamic Chord	c	0.3	m
Dihedral angle	Γ	2	degrees

3.2. Aerodynamic Model

The aerodynamic characteristics of an aerial vehicle are very important in determining the behavior and performance of an aircraft. In this work, the concern is more about the flight performance (i.e., range and endurance) of the aircraft itself rather than the dynamic behavior of the aircraft. This is due to the fact that range and endurance of the flight is affected by the aerodynamic efficiency $(C_L/C_D)_{max}$ and $\left({C_L}^{3/2}/C_D\right)_{max}$. These are the two factors determining the range and endurance performance of the aircraft, respectively.

The aerodynamic model used here assumes steady and laminar airflow. First of all, the aerodynamic characteristics of the aircraft are obtained from the result of the design process. There are two main characteristics: first is the coefficient of lift, C_L, and second is the coefficient of drag, C_D. These two characteristics are mainly determined by the airfoil profile used and the geometry of the aircraft itself. Table 6 summarizes the wing airfoil section properties. Figure 9 shows the shape of the wing airfoil.

Figure 9 SD7032 Airfoil

Table 6 SD7032 Aerodynamic properties [16]

SD 7032	
t/c	0.1
Cl_α	$6.0333 rad^{-1}$
α_{0l}	- 4.253 Deg
Cl_0	0.4485
Cl_{max}	1.554 (Re 500.10^3)

Symmetric airfoil is used for both vertical tail planes and horizontal tail planes. Both airfoils are NACA0010 which is commonly used for vertical and horizontal stabilizers. Table 7 summarizes the characteristics of this airfoil. This data was obtained from simulation using XFLR5. The $C_l - \alpha$ for the graph of NACA0010 is shown in Figure 11. Figure 10 shows the shape of the NACA0010 airfoil.

Figure 10 NACA 0010 Airfoil

Table 7 NACA0010 Aerodynamic Properties [16]

NACA 0010	
t/c	0.1
Cl_α	$6.07 rad^{-1}$
α_{0l}	0 Deg
Cl_0	0
Cl_{max}	0.9357 (Re $\approx 200.10^3$)

Based on these airfoils and the geometry of aircraft, the aerodynamic characteristics are determined through aerodynamic analysis during the design process.

The coefficient of lift, C_L, is a dimensionless coefficient that represents how much lift force can be generated by the lifting surface. Equation (1) defines the lift as a function of the C_L. There is a distinction between the coefficient of lift for a three dimensional wing and for the airfoil section. The C_L is used for expressing the coefficient of lift for a wing and C_l is used for a section of the wing or an airfoil. By evaluating this factor, one can have an estimate of how much lifting surface can

generate lift force regardless of the operating condition. This coefficient is a function of the flow angle of attack. Figure 11 and Figure 12 show how the angle of attack relate to the coefficient of lift of an NACA0010 airfoil and wing with an SD7032 airfoil. Both are obtained from an XFLR5 simulation. The NACA0010 and many others coordinates are available for public use at [17].

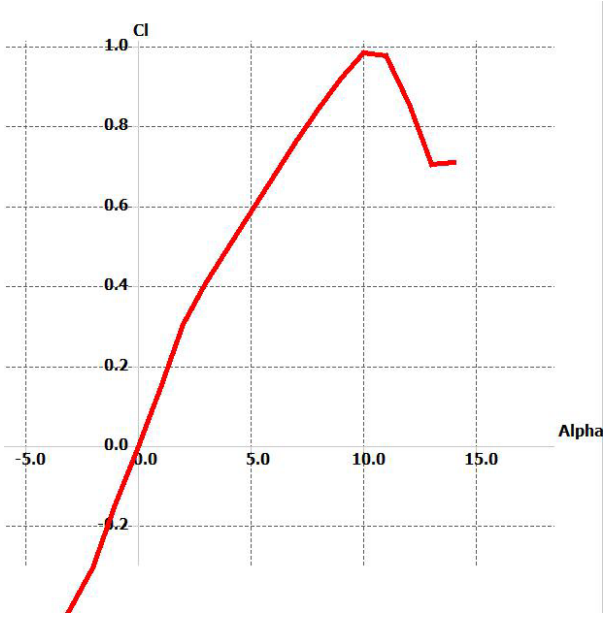

Figure 11 C_l – α for NACA0010

The coefficient of drag, C_D, is a dimensionless factor that represents how much drag force can be generated by a geometry when moving through the air. For a lifting surface, this coefficient is a function of the coefficient of lift as well due to induced drag (explained earlier). Figure 4 shows the relationship between the coefficient of drag and the coefficient of lift. Moreover, from this proposed aircraft design the drag polar and coefficient of lift function are defined by the following equation:

$$C_L = 4.4377\alpha + 0.3331 \quad \textbf{(7)}$$

$$C_D = 0.0792\, {C_L}^2 - 0.0359 C_L + 0.0188 \quad \textbf{(8)}$$

These functions are obtained from an aerodynamic simulation of the aircraft using XFLR5 software for a range of angles of attack at Reynolds number 420000. Figure 12 and Figure 13 show the C_L v.s α plot and the drag polar of the aircraft. The detailed data of these graphs are presented in Table 8. By setting a certain angle of attack value, the C_L and C_D can be determined by using those equations.

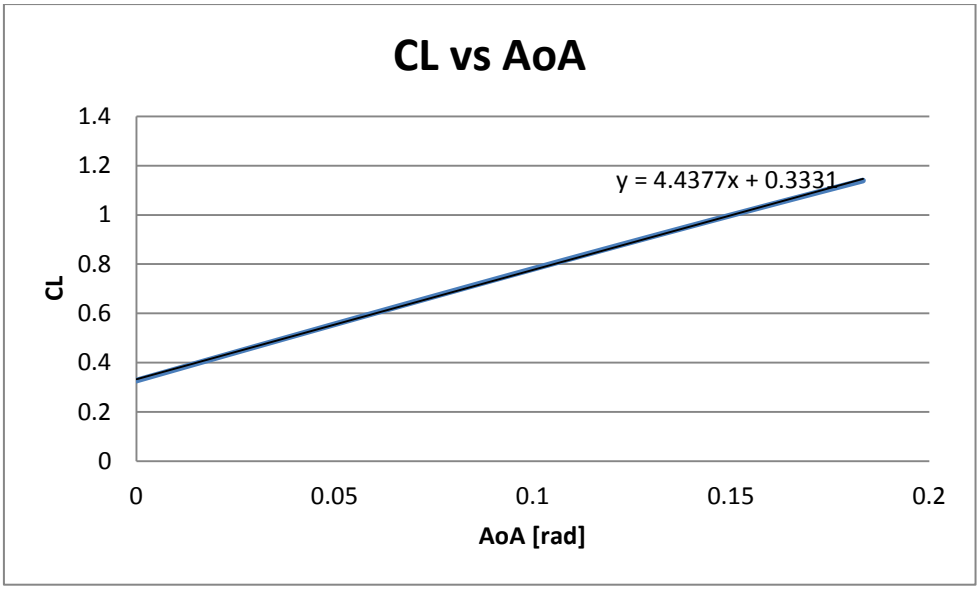

Figure 12 $C_L - \alpha$ of The Designed UAV

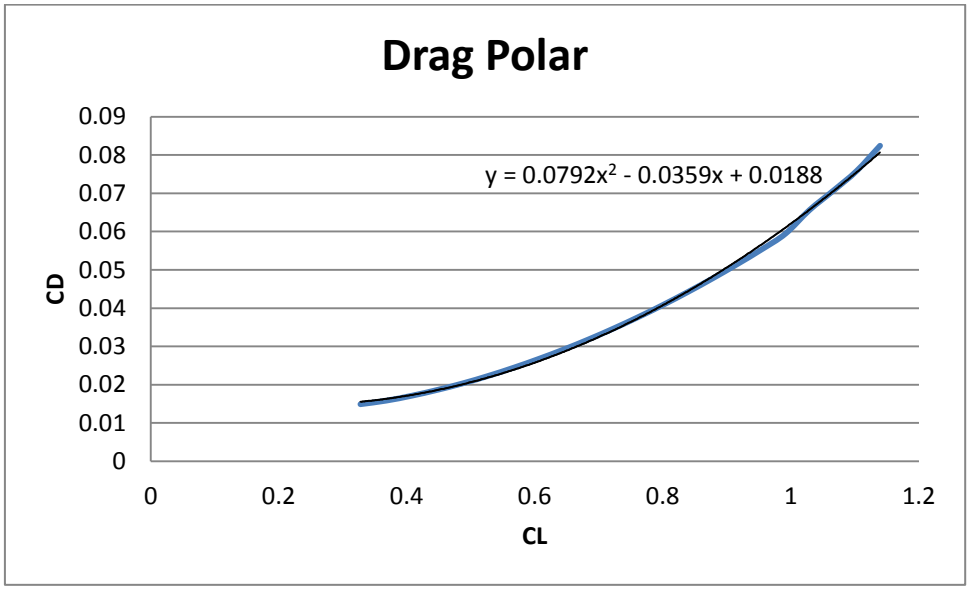

Figure 13 The Drag Polar Characteristics of The Designed UAV

Considering the assumption that most of the flight time is at cruising phase, the analysis has therefore been conducted for cruise condition. Therefore, at cruise condition the lift force generated is equal to the weight of the aircraft. The angle of attack of this aircraft is zero, although for different aircrafts the angle of attack at cruise condition may be not zero. Therefore, the minimum speed for the cruise can be defined using (9).

$$V_{min} = 1.2\left[\frac{2\ g\ m_{total}}{\rho S C_L}\right]^{0.5} \quad (9)$$

3.3. Propeller Model

In this section the modeling of the propeller is described. The method used for modeling the propeller is vortex theory. This method is similar to blade element momentum theory with a slight modification. The blade element momentum theory is the most common method used for analysis of the propeller. The vortex theory includes the effect of the induced velocity due to helical vortex of the rotating propeller.

The vortex theory of screw propellers approximates the propeller as a lifting surface and analyzes it as a lifting line. The lifting surface consists of a finite number of airfoil sections where the pitch angle, chord, and airfoil section are distributed as a function of the radius. Each section generates lift when the propeller blade is rotating with an angular velocity ω while advancing forward with relative velocity V_∞. Figure 6 describes the relation of angular velocity and advance velocity and the forces generated for each section.

When the propeller blade is rotating and advancing through the air, the resultant velocity has an angle of attack. With respect to the local airfoil, this angle of attack is reduced by induced velocity of the flow to α_b. This angle of attack is a function of aerodynamic pitch angle subtracted by the downwash angle, ε_b. Philips [14], defines the aerodynamic pitch angle as a function of chord line pitch angle, $\beta_c(r)$, subtracted by the zero lift angle of attack of the airfoil section, $\alpha_{L0}(r)$, located at the same radius, r.

$$\beta(r) = \beta_c(r) - \alpha_{L0}(r) \tag{10}$$

$$\alpha_b(r) = \beta(r) - \varepsilon_b(r) = \beta(r) - \varepsilon_\infty(r) - \varepsilon_i(r) \tag{11}$$

ε_∞ is called advance angle and is determined from the geometry as $\varepsilon_b(r) = \tan^{-1}\left(\frac{V_\infty}{\omega r}\right)$. ε_i is the induced angle. Thus, the resultant velocity relative to the cross-section is defined as V_b. As mentioned previously, this velocity is the result of the rotational velocity vector and forward velocity affected by an induced velocity, V_i . To be more specific, this induced velocity has two velocity components, $V_{\theta i}$ in θ direction and V_{xi} in x direction which is parallel to the rotational axis. Hence, the V_b at the blade section is defined as

$$V_b{}^2 = (\omega r - V_{\theta i})^2 + (V_\infty + V_{xi})^2 = \omega^2 r^2 \left[\left(1 - \frac{V_{\theta i}}{\omega r}\right)^2 + \left(\frac{V_\infty}{\omega r} + \frac{V_{xi}}{\omega r}\right)^2\right] \tag{12}$$

Equation (12) based on Figure 6 also can be written as

$$V_b = \sqrt{\omega^2 r^2 + {V_\infty}^2 \cos \varepsilon_i} = \frac{\omega r}{\cos \varepsilon_\infty} \cos \varepsilon_i \quad \textbf{(13)}$$

As can be seen in Figure 6, thrust, T, on the section is the axial component of the lift force subtracted by the axial component of the drag force generated by propeller blade section. The sectional lift is given by

$$\tilde{L} = \frac{1}{2} \rho {V_b}^2 c_b \widetilde{C_L} = \frac{1}{2} \rho \omega^2 r^2 c_b \widetilde{C_L} \left[\left(1 - \frac{V_{\theta i}}{\omega r} \right)^2 + \left(\frac{V_\infty}{\omega r} + \frac{V_{xi}}{\omega r} \right)^2 \right] \quad \textbf{(14)}$$

and the sectional drag force is given by

$$\widetilde{D} = \frac{1}{2} \rho {V_b}^2 c_b \widetilde{C_D} = \frac{1}{2} \rho \omega^2 r^2 c_b \widetilde{C_D} \left[\left(1 - \frac{V_{\theta i}}{\omega r} \right)^2 + \left(\frac{V_\infty}{\omega r} + \frac{V_{xi}}{\omega r} \right)^2 \right] \quad \textbf{(15)}$$

Hence, the thrust generated by the section can be expressed as

$$\tilde{T} = \tilde{L} \cos \varepsilon_b - \widetilde{D} \cos \varepsilon_b \quad \textbf{(16)}$$

The components of thrust and drag in circumferential direction are expressed as

$$\widetilde{F_\theta} = -\tilde{L} \sin \varepsilon_b - \widetilde{D} \cos \varepsilon_b \quad \textbf{(17)}$$

However, these two forces are only for one section at a radius of r. So the thrust and torque with respect to the radius can be expressed as

$$\frac{dT}{dr} = \frac{k_{blade}}{2} \rho \omega^2 r^2 c_b \left[\left(1 - \frac{V_{\theta i}}{\omega r} \right)^2 + \left(\frac{V_\infty}{\omega r} + \frac{V_{xi}}{\omega r} \right)^2 \right] \left(\widetilde{C_L} \cos \varepsilon_b - \widetilde{C_D} \cos \varepsilon_b \right) \quad \textbf{(18)}$$

The torque is the aerodynamic moment produced by the blade section with respect to the propeller rotation axis. Thus, the torque per unit radius is the product of circumferential force, radius r and the number of propeller blades.

$$\frac{dQ}{dr} = \frac{k_{blade}}{2} \rho \omega^2 r^2 c_b \left[\left(1 - \frac{V_{\theta i}}{\omega r} \right)^2 + \left(\frac{V_\infty}{\omega r} + \frac{V_{xi}}{\omega r} \right)^2 \right] \left(\widetilde{C_D} \cos \varepsilon_b + \widetilde{C_D} \sin \varepsilon_b \right) \quad \textbf{(19)}$$

The thrust and torque for the whole propeller can be found by integrating these two equations from hub to tip of the propeller. From Figure 6, the induced velocity components of the propeller's rotational axis and circumferential direction can be expressed as follows

$$V_i = \sqrt{\omega^2 r^2 + {V_\infty}^2 \sin \varepsilon_i} = \frac{\omega r}{\cos \varepsilon_\infty} \sin \varepsilon_i \quad \textbf{(20)}$$

$$V_{xi} = V_i \cos \varepsilon_b = \frac{\omega r}{cos\, \varepsilon_\infty} sin\, \varepsilon_i \cos(\varepsilon_i + \varepsilon_\infty) \quad \textbf{(21)}$$

$$V_{\theta i} = V_i \sin \varepsilon_b = \frac{\omega r}{cos\, \varepsilon_\infty} sin\, \varepsilon_i \sin(\varepsilon_i + \varepsilon_\infty) \quad \textbf{(22)}$$

Goldstein's vortex theory proposes that the $V_{\theta i}$ in the plane of the rotating propeller disk is related to the local circulation, Γ, given by

$$k\Gamma = 4\pi\kappa r\, V_{\theta i} \tag{23}$$

The term Kappa is a Goldstein's Kappa Factor which is only available in graphical form. Thus, for practical use the Kappa is approximated by using Prandtl's tip loss factor, expressed as

$$k\Gamma = 4\pi f r\, V_{\theta i} \tag{24}$$

$$f = \frac{2}{\pi}\cos^{-1}\left\{\exp\left[-\frac{k\left(1-2r/d_p\right)}{2\sin\beta_t}\right]\right\} \tag{25}$$

Based on potential flow theory, the Kutta-Joukowski theorem proposes that lift can be calculated by imposing a circulation around the airfoil section. For this particular application the relation is given by

$$\tilde{L} = \Gamma\rho V_b \tag{26}$$

Using equation (4), (5), and (17), the local section circulation can be rewritten as

$$\Gamma = \frac{1}{2}V_b c_b \widetilde{C_L} = \frac{1}{2}\omega r c_b \widetilde{C_L}\frac{\cos\varepsilon_i}{\cos\varepsilon_\infty} \tag{27}$$

Applying equation (13) and (18) into equation (15) yields the relation

$$\Gamma = \frac{1}{2}V_b c_b \widetilde{C_L} = \frac{1}{2}\omega r c_b \widetilde{C_L}\frac{\cos\varepsilon_i}{\cos\varepsilon_\infty} \tag{28}$$

$$\frac{kc_b}{16r}\widetilde{C_L} - \cos^{-1}\left\{\exp\left[-\frac{k\left(1-2r/d_p\right)}{2\sin\beta_t}\right]\right\}\tan\varepsilon_i \sin(\varepsilon_i+\varepsilon_\infty) = 0 \tag{29}$$

By knowing the propeller geometry, the section coefficient lift function, the rotational velocity and the forward velocity, (29) can be solved numerically to find the induced angle, ε_i, for every section with radius r.

The thrust and torque can be calculated by integrating equation (18) and (19) starting from hub to tip radius as expressed by

$$T = \int_{r=r_h}^{r_0}\frac{dT}{dr}dr \tag{30}$$

$$Q = \int_{r=r_h}^{r_0}\frac{dQ}{dr}dr \tag{31}$$

However, normally the performance parameters of the propeller are expressed in non-dimensional coefficients. The relations for non-dimensional coefficients are given by

$$C_T = \frac{T}{\rho(\omega/2\pi)^2 {d_p}^4} \quad \textbf{(32)}$$

$$C_Q = \frac{Q}{\rho(\omega/2\pi)^2 {d_p}^5} \quad \textbf{(33)}$$

$$C_P = \frac{Q\omega}{\rho\left(\omega/_{2\pi}\right)^3 {d_p}^5} \quad \textbf{(34)}$$

$$\eta_p = \frac{TV_\infty}{Q\omega} \quad \textbf{(35)}$$

$$J = \frac{V_\infty}{\left(\omega/_{2\pi}\right) d_p} \quad \textbf{(36)}$$

where C_T is the coefficient of thrust, C_Q is the coefficient of torque, C_P is the coefficient of power, η_p is the propeller efficiency, and J is advance ratio.

However, in order to obtain more accurate results of propeller aerodynamic performance, an artificial neural network (ANN) is used. The modeling is based on the performance data provided by the manufacturer [18]. The data consists of several sizes of two-blade electric propellers made by APC. The diameter range is from 15 to 27 inches with pitch ranging from 10 to 15 inches. The available propeller data is at multiple advance ratios, J, and yields the corresponding thrust coefficient, C_T, and power coefficient, C_P. The ANN model of the propeller is trained using advance ratio, J, and pitch to diameter ratio, Kc. The required outputs are C_T and C_P for which the ANN model is built separately. Figure 14 illustrate how the ANN model for each C_T and C_P is built.

The artificial neural network (ANN) model of the propeller is implemented by using the SUMO (Surrogate Modelling) toolbox developed by D. Gorissen [19] and his team from Gent University of Belgium. The SUMO toolbox utilizes the Matlab Neural Network toolbox with a default configuration of ANN. The training method is Bayesian Regulation, where the hidden layer is based on the tan-sigmoid model and the output layer is based on pure linear model. Figure 16 and Figure 17 show the plot of C_T & C_P produced by the ANN model of the propeller for different values of advance ratio, *J*, and pitch to diameter ratio, Kc

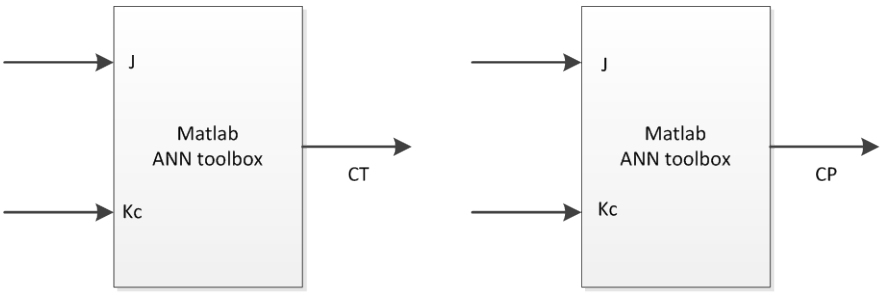

Figure 14 Modeling Propeller using Matlab's ANN Toolbox

In Figure 15, graph shows the comparison of these two approaches of modeling of the propeller with regard to the manufacturer data. Figure 16 is an example of a two-blade propeller with a 16 inch diameter and an 8 inch pitch.

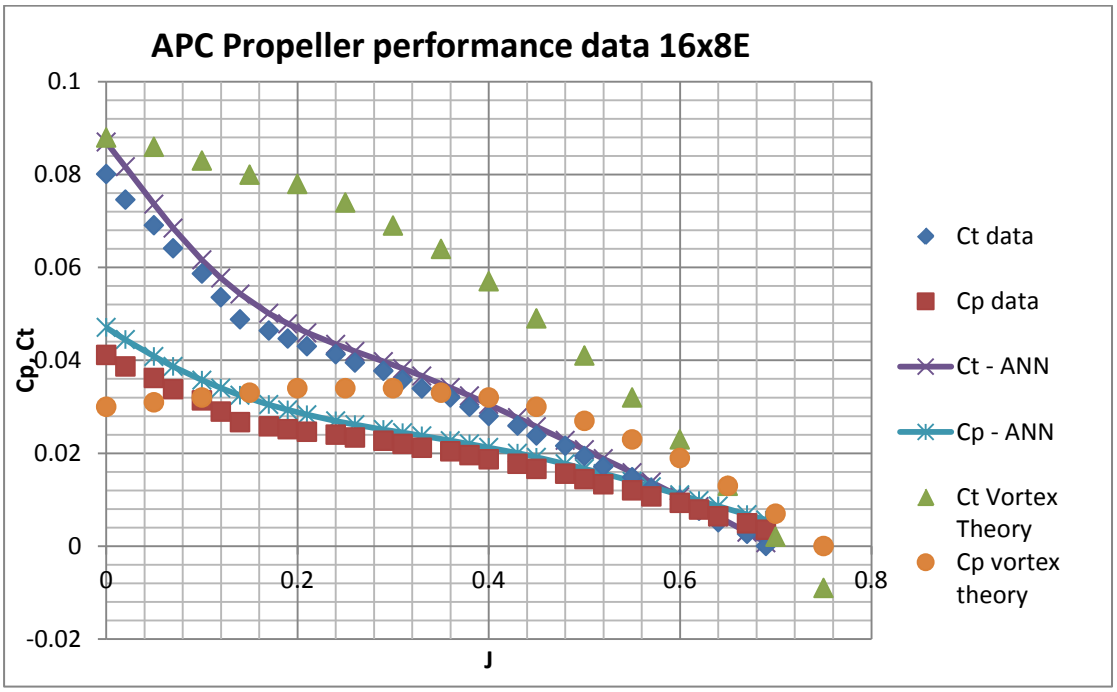

Figure 15 16 x 8E Propeller Performance

As can be seen in Figure 15, the vortex theory has very big discrepancy with the provided data from the manufacturer. The artificial neural network (ANN) model has a better result and closely matches the manufacturer data. Thus, in the next section this ANN is preferred in the analysis and optimization.

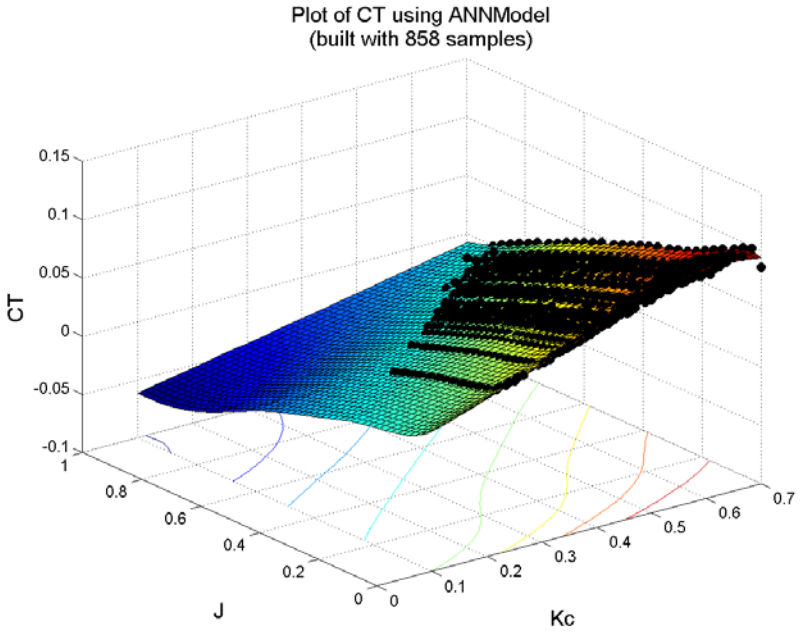

Figure 16 Plot of CT using ANN Model

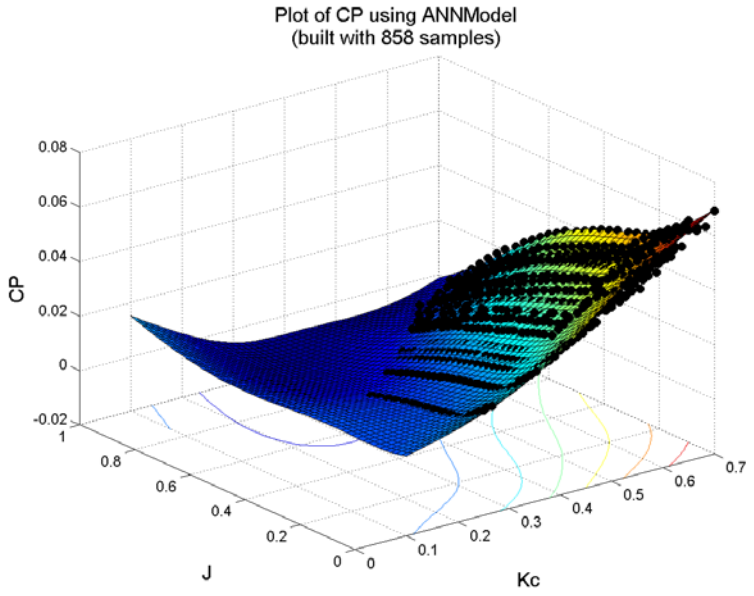

Figure 17 Plot of CP using ANN Model

3.4. Electric Motor

In order to spin the propeller, an electric motor is required. In aeronautical applications, the most commonly used electric motor is a brushless DC motor. This motor has advantages over a brushed DC motor including a higher power density, higher dynamic response, longer operating life, higher efficiency, and higher speed range. The electric DC motor model is built for steady state conditions because the

focus is to optimize the performance of the propulsion system during cruise conditions which mostly use a constant duty cycle.

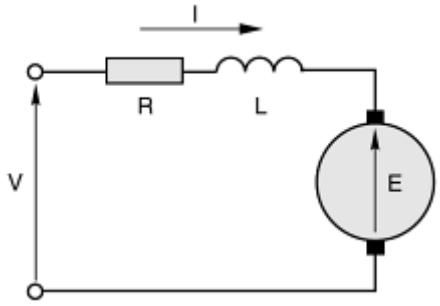

Figure 18 Brushless DC Motor Simplified Model

The model uses load current, I_m, winding resistance, R_m, input voltage, V_t, and voltage constant, K_v. The relation is given by

$$V_t = E_m + 2R_m I_m \quad \textbf{(37)}$$

$$E_m = K_b \omega_m \quad \textbf{(38)}$$

The R_m is multiplied by a factor of two because each commutating sequence requires two windings in series [5]. For steady state conditions, the torque of the motor is given by

$$Q_m = K_t I_m \quad \textbf{(39)}$$

K_b is the back EMF constant which in S.I. units is equal to the torque constant, K_t. Therefore, equations (37) to (39) can be simplified to

$$Q_m = \frac{(V_t - K_b \omega_m)}{2R_m} K_t \quad \textbf{(40)}$$

And K_t is inversely proportional with voltage constant K_v

$$K_v = \frac{\omega_m}{V_t} = \frac{1}{K_t} \quad \textbf{(41)}$$

In some applications, the DC motor is equipped with a gearing mechanism in order to change motor shaft rotational speed, usually to reduce the rotational speed. Because of that, the K_v is reduced. Therefore, for the DC motor that uses gearing with a gear ratio more than one, G_r, equations (38) and (39) can be rewritten as

$$E_m = K_b \omega_m G_r = \frac{\omega_m G_r}{K_v} \quad \textbf{(42)}$$

$$Q_m = K_t I_m G_r = \frac{I_m G_r}{K_v} \quad \textbf{(43)}$$

Refering to [5], under no-load conditions, the motor can also suffer a loss due to windage and friction. To incorporate this effect, a motor drag coefficient is calculated. The motor drag coefficient, β, is given by

$$\beta = \frac{\left(\frac{K_v}{G_r}\right)^2 I_0}{V_0 - 2R_m I_0} \quad (44)$$

where I_0 is the no-load current and V_0 is the corresponding no-load voltage; both are typically supplied by manufacturer. Thus, the torque equation (39) should be corrected by the no-load condition in order to ensure that the motor model passes through the no-load condition.

$$Q = Q_m - \beta \omega_m \quad (45)$$

Applying equations (43) and (44) into equation (45), we can obtain

$$Q = \frac{I_m G_r}{K_v} - \beta \omega_m \quad (46)$$

3.5. Motor Speed Controller

A brushless DC motor requires an external controller for switching the commutating sequence. The controller gives a duty cycle that is driven by a command from the pilot transmitter or an autopilot. The duty cycle, D_c, determines how much current is delivered to the motor. Lindahl [5] proposes that the controller can be modeled with the assumption that the losses of the controller are neglected, as follows:

$$V_t = D_c V_p \quad (47)$$

$$I_m = \frac{1}{D_c} I_p \quad (48)$$

where the duty cycle value range is between 0 to 1. Moffit [3] says that for simple systems where there are no auxiliary loads connected to the propulsion power source, the propulsive current and voltage would be exactly equal to the power source current and voltage. The V_p and I_p refer to the voltage and current the power source required to produce the propulsive force on the aircraft.

However, according to Moffit [3] the motor voltage relation equation (47) should be modified to include the efficiency and resistance terms of the controller. This is because practically, the near lossless condition is only achieved when the duty cycle is near one or full throttle. The modified relation is given by

$$V_t = \eta_{cont} D_c V_p - I_m R_{cont} \quad \textbf{(49)}$$

R_{cont} is the controller resistance value which is provided by the manufacturer, and η_{cont} is the controller efficiency. Moffit also suggested, for simplicity, that the efficiency increase can be treated as linear with the duty according to

$$\eta_{cont} = 1 - k_{loss}(1 - D_c) \quad \textbf{(50)}$$

where k_{loss} determines the rate of the efficiency decrease as the duty cycle decreases. According to Phillips [20] from the experience that he has gained, the suggested k_{loss} value is 0.078.

3.6. Fuel Cell Model

The fuel cell model that is used here is the fuel cell polarization curve of current and voltage. The mathematical model is obtained from the quadratic curve fitting from scattered data gathered from the Aeropak™ fuel cell data log. The data is obtained by an experimental test of the Aeropak™ fuel cell with the load until it reaches the full range of operating power. Figure 19 shows the polarization curve of the Aeropak™ fuel cell as a quadratic curve fit from the test data.

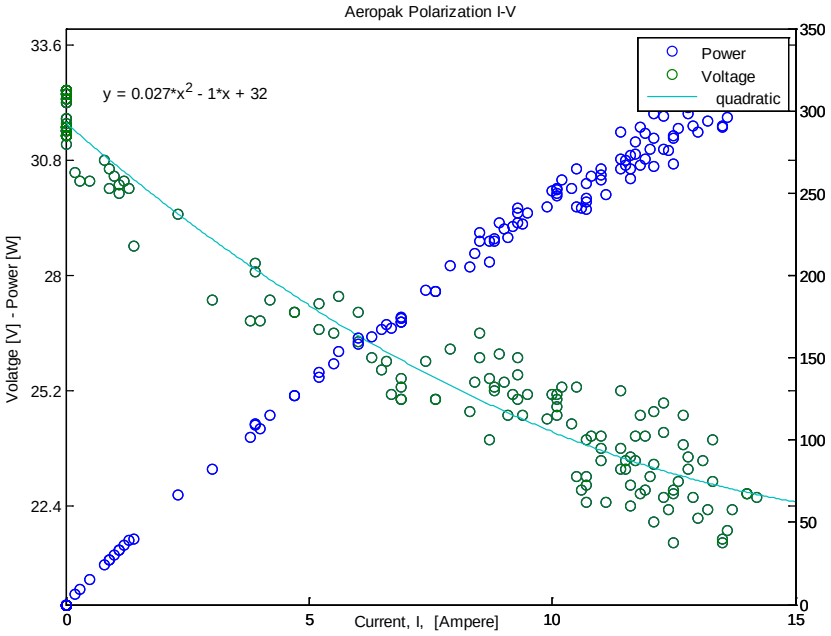

Figure 19 Aeropak Polarization I-V

The quadratic curve fit shows the relation between the Aeropak voltage with the current produced and defined by

$$V_{fc} = 0.027{I_{fc}}^2 - I_{fc} + 32 \quad \textbf{(51)}$$

The current produced by the fuel cells determines the hydrogen consumption rates. The relation between hydrogen consumption and the fuel cell current is given by Faraday's law, as described in equation (52), where U_{H2} is the hydrogen utilization factor which has a value between 0 and 1.

$$\dot{N_{H2}} = \frac{N_{cells} I_{fc}}{2 U_{H2} F} \tag{52}$$

By knowing the hydrogen consumption rate, the amount of hydrogen consumed can be determined. Once the hydrogen consumption is known, the endurance of the aircraft can be determined. The amount of stored hydrogen is determined by the ideal gas law in equation (53). The hydrogen utilization factor is the ratio between the fuel flow that reacts and the input fuel flow. According to [21] the typical value used is between 0.8 to 0.9. Equation (53) is as follows:

$$PV = n\,RT \tag{53}$$

where *P* is pressure contained in the H_2 tank, V is the volume of H_2 storage, R is ideal gas constant, T is the temperature, and n is the amount of H_2 in moles. This amount of H_2 divided by the consumption rate yields the time, after which the endurance of the air craft can be predicted. Figure 20 shows the Aeropak fuel cell system used in this work.

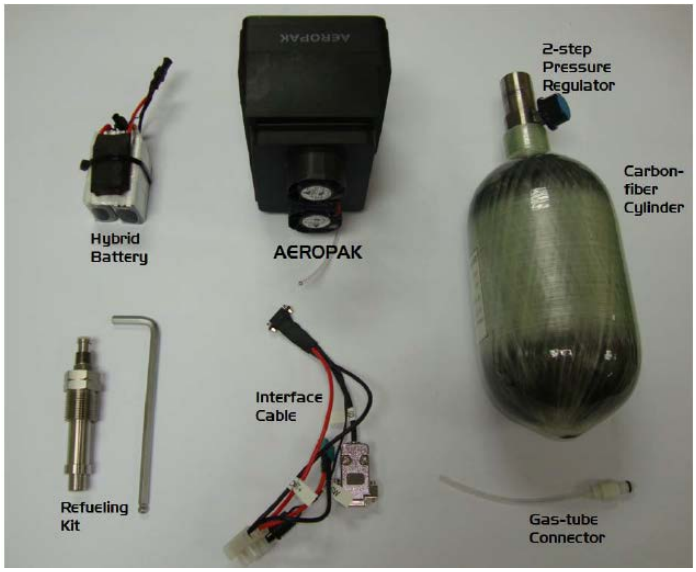

Figure 20 Aeropak Fuel Cell System [22]

3.7. Flight Performance

As mentioned previously, the aircraft is assumed to be flying at cruise condition at a steady level of flight. The two important flight performance parameters are range and endurance. However, the range of a UAV is also limited by the

communication capability of the on-board communication system and the ground controller. Endurance is defined as the total flight time that can be achieved by the aircraft to stay in the air on the maximum amount of fuel that can be carried on board. The range is defined as a horizontal straight-line distance of an airplane travelling in cruising flight [22].

In steady level flight, the power available must be equal to the power required.

$$P_{required} = P_{available} \tag{54}$$

The power required and the power available are defined as

$$P_{required} = DV \tag{55}$$

$$P_{available} = TV \tag{56}$$

By knowing the power required, the thrust available by the propulsion system can be determined. The thrust is defined by equation (57)

$$T = C_T \rho {d_p}^4 \left(\frac{\omega}{2\pi}\right)^2 \tag{57}$$

where C_T is the coefficient of thrust, ρ is air density, d is propeller diameter and ω is rotational speed of the propeller. To provide the required thrust, a certain current and voltage level from the fuel cell is required. In order to maintain a certain output power produced by the fuel cell, a certain hydrogen flow rate is required as well. By knowing the required hydrogen flow rate, hydrogen utilization and amount of hydrogen stored, the endurance of a steady level flight can estimated. This is with assumption that the mass of aircraft does not change during the flight because the mass of compressed hydrogen gas is very small compared to the total weight of the aircraft.

Rujigrok in [22] derives that the range can be expressed as shown in equation (58)

$$R = \frac{\eta_j}{c_P}\frac{C_L}{C_D}\ln\frac{W_1}{W_2} \tag{58}$$

where η_j is propulsive efficiency, c_P is the specific fuel consumption, ans W_1 and W_2 are the initial cruise weight and final cruise weight, respectively. Aerodynamically, the maximum range can be achieved if the C_L/C_D is at maximum. Therefore, for the maximum range analysis, the aircraft flight condition should be trim at an angle of attack that gives this maximum (C_L/C_D).

The same author in [22] also states that maximum endurance is achieved when the flight condition requires minimum power. The relation of the endurance based on [22] is expressed as

$$E = \frac{\eta_j}{c_P}\sqrt{\frac{{C_L}^3/{C_D}^2}{\frac{2}{S\rho}}}\left[\frac{2}{\sqrt{W_2}} - \frac{2}{\sqrt{W_1}}\right] \quad \textbf{(59)}$$

Based on equation (58) the endurance can be maximized if the aircraft flies at the angle of attack of which ${C_L}^{3/2}/C_D$ is the maximum. Table 8 shows the value of the angle of attack and the corresponding C_L, C_D, C_L/C_D, and ${C_L}^{3/2}/C_D$.

Table 8 Aerodynamic performance of the designed aircraft

alpha		CL	CD	CL/CD	$CL^{3/2}/CD$
deg	rad				
0	0	0.327573	0.014906	21.97592	12.57769
1	0.017453	0.407688	0.017121	23.81216	15.20417
2	0.034907	0.487458	0.020354	23.949	16.72076
3	0.05236	0.566796	0.024436	23.19512	17.46265
4	0.069813	0.645613	0.029233	22.08508	17.74537
5	0.087266	0.723825	0.03474	20.83549	17.7264
6	0.10472	0.801344	0.040933	19.57697	17.52487
7	0.122173	0.878088	0.047799	18.37043	17.21426
8	0.139626	0.953976	0.055292	17.25342	16.85171
9	0.15708	1.028926	0.065588	15.68772	15.91299
10	0.174533	1.102862	0.075841	14.54177	15.27136

Table 8 shows that for the best range, the aircraft should fly at a 2 degree angle of attack since the C_L/C_D at this point is the highest. For the maximum endurance, however, the aircraft should fly at a 4 degree angle of attack. This angle of attack is limited by the stall mentioned earlier in section 3.2.

Assuming that the thrust line is aligned with the fuselage reference line, the thrust, drag, lift and weight relation can be described in Figure 21. The relations are given by the following equations from equation (60) to (61).

$$T - D - W\sin\gamma = 0 \quad \textbf{(60)}$$

$$L - W\cos\gamma = 0 \quad \textbf{(61)}$$

Using the relationship in equations (1) and (2) then substituting them with equations (55) and (61), the following relation can be obtained. γ is the flight path angle of the aircraft.

$$V = \left[\frac{2\ g\ m_{total}}{\rho S C_L}\cos\gamma\ \right]^{0.5} \quad \textbf{(62)}$$

$$D = \frac{C_D}{C_L} W \cos\gamma \quad \textbf{(63)}$$

From equations (60) and (63) the thrust required can be expressed as

$$T = W\left(\frac{C_D}{C_L}\cos\gamma + \sin\gamma\right) \quad \textbf{(64)}$$

Since the aircraft is assumed to be in steady cruise flight at constant altitude conditions, the flight path angle, γ, is equal to zero.

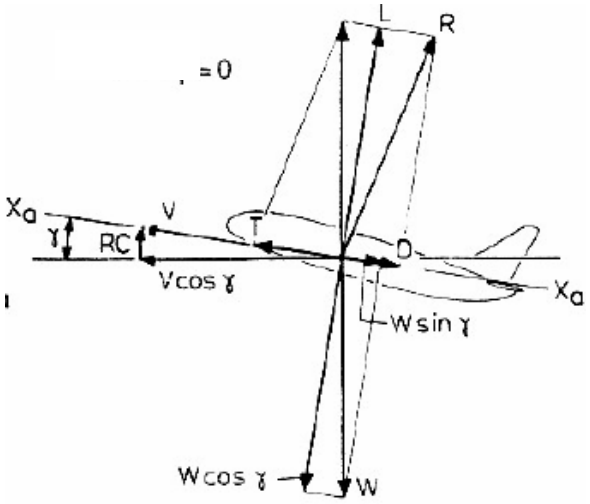

Figure 21 Aircraft in Steady Cruise Flight [22]

3.8. Multi-Disciplinary Analysis

This section describes how the analysis for the entire systems was carried out. Since the there is no closed form mathematical relation for the entire system involving non-linear equations, a simultaneous system analysis was used combined with a non-linear equation solver and compatibility equations.

This analysis involves an exchange of information between many disciplines. The analysis is structured in such a way that the information flows from one discipline to the other consecutively. The diagram in Figure 22 portrays the design structure matrix that describes how the analysis was carried out. The implementation of this analysis structure is illustrated in Figure 24.

Each box represents the analysis for a different design parameter. The lines on the top diagonal represent the feed forward information. The vertical line means input

information and the horizontal line means output that the feed forwarded. The lines on the low diagonal are the feedback information.

The solver variables are fuel cell voltage,V_{fc}, fuel cell current I_{fc}, and propeller coefficient of thrust, C_T. These variables are used as the inputs to the multi-disciplinary analysis. Those variables are initially set with some initial guessed values. Then these values are feed forwarded to each corresponding block in order to calculate the other design parameters.

First of all, the aircraft aerodynamic block determines C_L, C_D, cruising speed, and the drag force or required thrust, T_{req}, which refer to equations (2), (7), (8), and (9) for a predefined angle of attack that is set by the user at cruise condition. Then T_{req} is used in the calculation of propeller speed, ω, as defined in equation (32) with the C_T value obtained from the input variable. The advance ratio, J, is calculated in the subsequent block using the cruising speed parameter (calculated earlier) and propeller speed, ω, as defined in equation (36). The advance ratio and pitch to diameter ratio, K_c, are used as input to find the new value of C_T and C_P from the ANN model of the propeller. With the new value of ω and C_P, the propeller torque can be calculated. Assuming that the power of the propeller and the motor are the same and the gear ratio is 1, the motor current and voltage can be determined using equations (37) and (46). The fuel cell voltage, V_{fc}, is determined using its polarization curve in equation (51) with the fuel cell current value, I_{fc}, determined from the input variable.

The fuel cell current value, I_{fc}, is then calculated by assuming the efficiency of the motor speed controller is 1. Therefore, the power delivered from the fuel cell is the same as the motor power. Dividing the motor power with the new V_{fc} value yields the new value of I_{fc}. These new input variable values are then used in the compatibility equation to be used as the feedback for the nonlinear solver which is an fsolve function in Matlab. The solver will iterate the input variables until the compatibility equations are driven as close as possible to zero. Since fsolve (a nonlinear system of equations solver function available in Matlab®) is solving the problem iteratively, the user provides an initial guess value for each input variable.

In order to have a reasonable solution in the optimization part, some constraints were applied to the outer loop, specifically on the optimization part. In the next section this matter is discussed in more detail. Only some of the parameters that

were calculated in this analysis were used in the evaluation function of the genetic algorithm. They are the endurance, motor and propeller efficiency, fuel cell current and propeller tip Mach number.

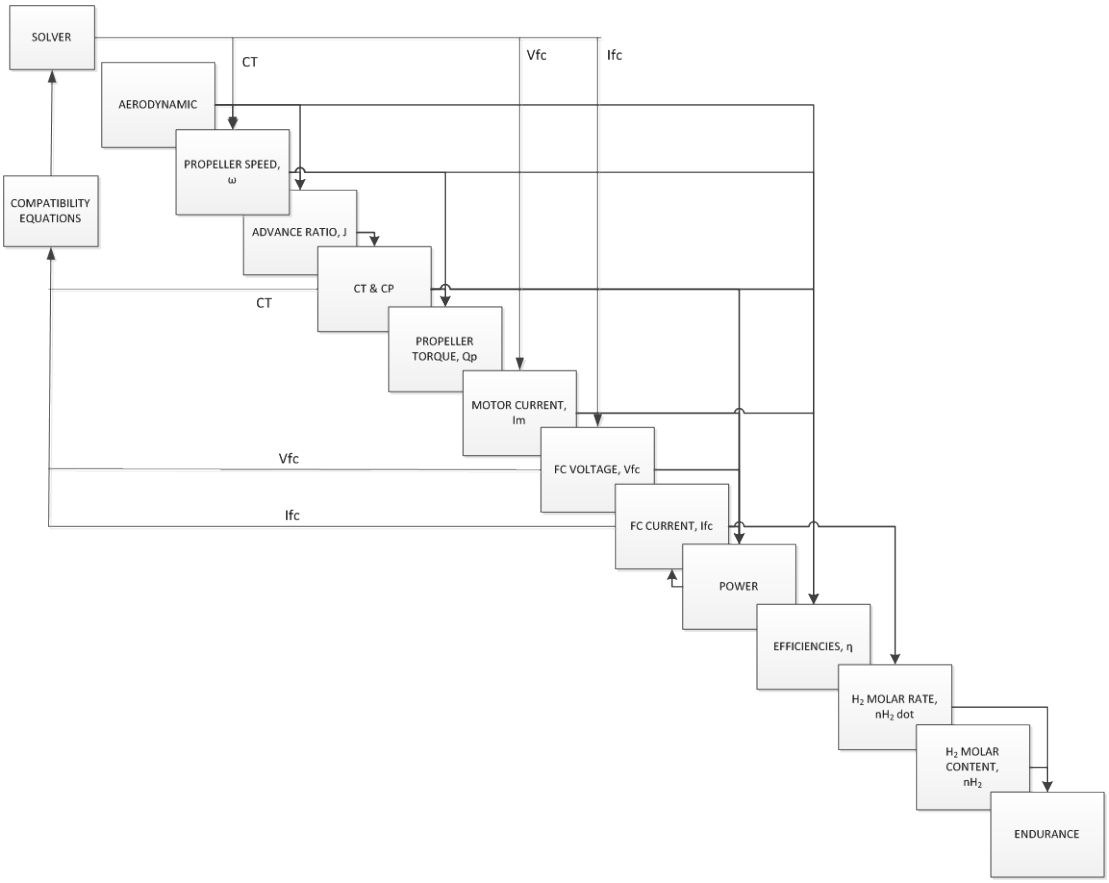

Figure 22 Multi-disciplinary Analysis Structure

The solver that is used to solve the nonlinear system in this work is a function called “fsolve” in Matlab. This fsolve function finds a solution system of nonlinear equations iteratively, specified by

$$F(x) = 0 \tag{65}$$

By default, fsolve uses the trust region dogleg method for solving nonlinear systems. It minimizes the merit function which is needed to decide if x_{k+1} is better or worse than x_k. The solver finds the values of input variables which are the roots of the system of nonlinear equations that satisfy equation (65). To define the problem as equation (65), compatibility equations are used. The compatibility equations used are

$$F_1(x) = \frac{V_{fc_{new}} - V_{fc_{old}}}{V_{fc_{old}}} \tag{66}$$

$$F_2(x) = \frac{I_{fc_{new}} - I_{fc_{old}}}{I_{fc_{old}}} \quad (67)$$

$$F_3(x) = \frac{C_{T_{new}} - C_{T_{old}}}{C_{T_{old}}} \quad (68)$$

Last, those three equations were set as $F_1(x) = 0$, $F_2(x) = 0$ and $F_3(x) = 0$ respectively. The nonlinear system of equations is implicitly solved if the compatibility equation is driven to zero.

3.9. Optimization Using Genetic Algorithm

Since the objective of this work is to find the optimized solution of propulsion for the given fuel cell, an optimization design approach was performed. The design problem involves a mixture of discrete and continuous values of design variables. These are motor index, propeller pitch length (p), propeller diameter (d_p), and motor gear ratio (GR). Motor index is basically an integer-identifier of a motor for which each of the motors have a different set of property parameters: property parameters include voltage constant, Kv, and no load current and voltage, I0 and V0. The propeller pitch and diameter are integer values used for propeller specifications in commercially available propellers. The gear ratio is a continuous design variable in which the value is assumed not to be limited to the availability of the gearbox in the market since it can be customized relatively to the specific needs. Since the data of the motor and propeller are obtained from the market, this involves many possible combinations of the motor and propeller. Moreover, there is no closed form mathematical solution to optimize and evaluate the objective function which in this case is the endurance of the flight. So the problem definition of the optimization here is classified as “mixed discrete continuous.” One of the solutions for solving this kind of optimization problem is the genetic algorithm.

Genetic algorithm development was pioneered by John Henry Holland from the University of Michigan in the 1970’s and has become very popular among researchers as a method used in optimization, artificial intelligence and machine learning [10]. The idea is inspired by the process of biological evolution theory. The reproduction of the new generation replaces the whole population of the old generation. The reproduction process is performed by means of recombination or crossover of the parent’s chromosomes and the stochastically triggered mutation. The

artificial chromosome is composed by encoding the decimal value of the design variable to a binary string.

The process is started by initializing a set of population of design entities with a different combination of design variable values that is randomly generated. The design variable value is then translated into a binary set of chromosome as shown in Table 9. Each chromosome is scored based on its fitness function value evaluation. The fitness function is the only link between the GA and its optimization problem that is being solved.

The score is a measure of the suitability of a solution to the problem. Then if the whole population satisfies the termination criteria, the process is stopped. If not, then a new generation is created. The parents are selected randomly with selection opportunities biased in relation to evaluations of the chromosome. The parent for subsequent generation is selected and the children are made by a crossover and mutation process of each parent chromosome. The offspring get different combinations of chromosome sets from their parents. The crossover plays an important role in a genetic algorithm since it can combine the solutions on different chromosomes and accelerate the search. Random mutations introduce randomness in the solution which can help to find solutions that might be overlooked by crossover alone.

The acceptance places the new children into a new population. After a new population is created, it is again evaluated according to the fitness function. Once the termination criteria are meet then the process of evolution is stopped. This process is illustrated in Figure 23.

Matlab has a genetic algorithm and direct search toolbox which are used in this work for implementing the optimization procedure. The multi-disciplinary analysis act as the evaluator function in the GA optimization routine. Figure 24 illustrates the structure of the whole process of optimization. The structure in Figure 22 is implemented in the multi-disciplinary analysis.

However, in order to guarantee feasibility of the solutions obtained from the optimization process, some design constraints were imposed. The constraints are the efficiency of the motor and propeller, fuel cell current and propeller tip Mach number. These four values are evaluated in every process analysis of design entities when the evaluation process of the GA is conducted. If the solution does not satisfy the

predefined constraints, the solution is discarded as a member of the population for the subsequent generation. Thus the creation of the new population is based on the members that met the evaluation criteria and were most feasible according to the constraints among the population of the previous generation. Table 12 in section 4.4 gives an example of how the imposed constraints were defined.

Table 9 Chromosome Set

Reference area, Sref [m^2]			Cruise speed, v [m/s]		
S1	8	1000	v1	11	1011
S2	7	0111	v2	10	1010
S3	5	0101	v3	9	1001
S4	9	1001	v4	12	1100

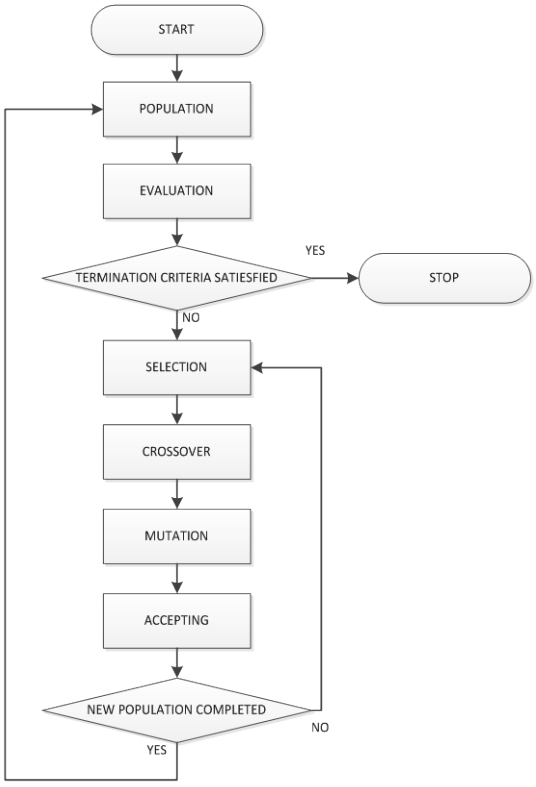

Figure 23 The Flowchart for The Genetic Algorithm

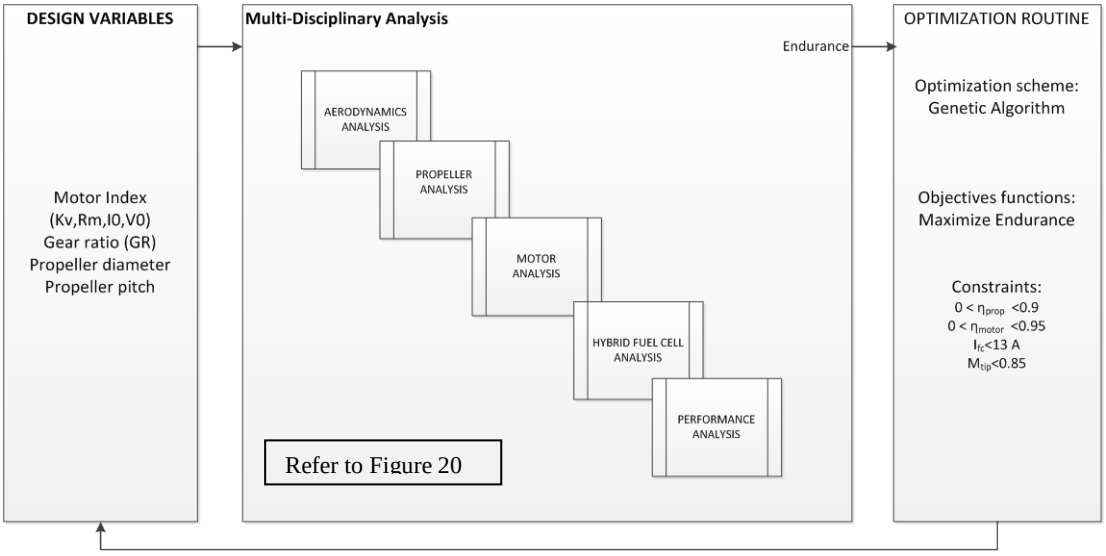

Figure 24 Optimization Structure

4. Design Optimization of the Propulsion System

In this chapter the implementation of the design and optimization of the propulsion system is presented. The validation results conducted in the wind tunnel test are presented as well. The implementation of the design and optimization methodology start with defining the problem setup. The setup defines the flight mission profile, design variables, objective function, optimization constraints and selection of the components. For this implementation, the motors and propellers were selected from commercially available components.

Wind tunnel experiments were conducted for validating the results of the optimization process. A wind tunnel was used to mimic the real load on the propeller at the real operating condition of the unmanned aerial vehicle. Thus, by conducting this experiment, the model of the propulsion system could be evaluated near its operating condition.

4.1. Implementation of Design Optimization

The flight profile considered here is a steady level flight at cruising speed where the speed and altitude are constant. The altitude is 1000 m above the sea level. The climb and descent are not considered here since it is a relatively low altitude flight, and thus the time to climb and descend is insignificant compared to the total endurance.

There are three scenarios considered in the present study. First is the cruise flight at the design speed of 19 m/s at an angle of attack zero. The second one is the cruising flight at $(C_L/C_D)_{max}$ which is at an angle of attack of 2 degrees. This condition is set to achieve the maximum range. The last scenario is the cruising flight at $\left(C_L^{3/2}/C_D\right)_{max}$ which is at a 4 degree angle of attack.

The motors that are used in the present study were limited to Hacker Motor series A40 to A60. These motors were chosen because they have wide range of Kv from 149 to 1100 RPM per volt. Moreover, one of the series was already available in the lab. Table 10 shows the list of the motor specifications used in the optimization. Besides the Kv, I0, V0, and Rm, the weight of each motor was also considered in the optimization.

The propeller size used in the study ranged from 15 to 27 inches in diameter with a pitch range from 7 to 15 inches. The last design variable is the gear ratio of the

gear reducer. This gear is used to reduce the rotational speed of the motor to match its rotation with the propeller rotational velocity.

Table 10 Hacker Motors A40, A50, and A60 Series

Motor Name	Index	Kv [RPM/V]	I0 [A]	Rm [Ohm]	Mass [g]	V0 [Volts]
A60 18L	1	149	1.6	0.016	658.6506	8.4
A60 16L	2	168	1.8	0.018	658.6506	8.4
A60 20M	3	170	1.7	0.032	576.6123	8.4
A60 18M	4	190	1.8	0.027	576.6123	8.4
A60 14L	5	192	2.5	0.02	658.6506	8.4
A60 24S	6	200	1.3	0.038	492.23	8.4
A60 16M	7	215	1.9	0.022	576.6123	8.4
A60 22S	8	215	1.5	0.03	492.23	8.4
A60 20S	9	235	1.8	0.027	492.23	8.4
A50 16L	10	270	1.7	0.031	389.0961	8.4
A50 14L	11	310	1.9	0.025	389.0961	8.4
A50 12L	12	355	2.3	0.021	389.0961	8.4
A50 16S	13	380	2	0.026	307.0578	8.4
A50 12S	14	500	2.5	0.016	307.0578	8.4
A50 10S	15	580	3.1	0.012	307.0578	8.4
A40 10L	16	600	2.4	0.018	260.1787	8.4
A40 12S	17	730	2.7	0.01	220.3315	8.4
A40 8L	18	750	3.1	0.013	260.1787	8.4
A40 10S	19	880	3.8	0.007	220.3315	8.4
A40 6L	20	1000	4	0.01	260.1787	8.4
A40 8S	21	1100	4.9	0.005	220.3315	8.4

The gear ratio has a range from 1 to 10. It is assumed that the gear reducer efficiency is 1. Table 11 summarizes the problem setup used in the optimization.

Table 11 Problem Setup Summary

Design Variables	Values	Units
Motor Index	1 to 21	unit less
Propeller Diameter	15 to 27	inch
Propeller Pitch	10 to 15	inch
Gear Ratio	1 to 10	unit less
Flight Condition		
Altitude	100	m
Angle of Attack	0,2,4	degrees
Air Density	1.215	kg m^{-3}
Hydrogen Content		
Fuel Tank Pressure	150	bar
Fuel Tank Volume	1.1	L
Hydrogen Utilization	0.85	unit less

4.2. Constraints and Objective Function

The optimization is driven to achieve the objective of maximizing the endurance of the aircraft at a steady level flight. However, there are several constraints that the optimization is subjected to. These constraints are imposed in order to get a feasible solution. They are defined in Table 12.

Table 12 Optimization Objective Function and Constraints

Minimize Objective Function	$-Endurance$
Subject to constraints : η_{motor} – is the motor efficiency $\eta_{propeller}$– is the propeller efficiency I_{fc} – is the fuel cell current M_{tip} - is the propeller tip Mach number	$0 < \eta_{motor} \leq 0.95$ $0 < \eta_{propeller} \leq 0.9$ $I_{fc} \leq 13\ A$ $M_{tip} \leq 0.85$

The genetic algorithm in Matlab is designed to minimize the objective function; therefore, in order to achieve the maximum endurance, a negative sign was added to the value of the endurance in the objective function. The constraints of efficiency of motor and propeller were set in order to insure the legitimacy of the design [9]. The current of the fuel cell was limited to the 13 amperes to prevent the overloading of the fuel cell stack when connected to the motor. The propeller tip Mach number accounts for the compressibility effect and limits the rotational propeller speed.

4.3. Experimental Test

The entire experimental test was conducted in the open circuit low speed wind tunnel as shown in Figure 25. The wind tunnel was designed for 40 m/s maximum airspeed at the test section. The test section cross section size was 90 by 72 centimeters. A test stand was mounted in the test section as shown in Figure 26. The mount was connected with a load cell to measure thrust force produced by the propeller. The motor used in the experimental test was the hacker C50 15XL with a 6.7 to 1 gearbox. It has Kv of 1160 without gearbox and the combined actual Kv becomes 173.1343 RPM/volt if with the gearbox [23]. This motor specification is the closest to the one obtained by the optimization result as discussed in part 4.4 and was chosen based on the availability of the components in the lab. The same approach also applied to the propeller. There were three different propellers used in the test. Their

specifications were close to the optimization solutions. Their sizes were 16 by 11, 17 by 10, and 20 by 13 inches. They were selected based on the closest specification to the solution found in the optimization for each scenario. Since at the time of the experiment the fuel cell had electrical problems, a regulated power supply was used as the power source instead. Therefore, the actual endurance test could not be established due to the technical difficulties with the Aeropak™ fuel cell module.

Figure 25 Open Circuit Wind Tunnel

The instruments used in this experiment are described in this section. The load cell from ELFF-T2M-100N from Measurement Specialties was used to measure thrust force with a maximum load of 100 N. The pressure transducer MPXV7002 was used for measuring the dynamic pressure in the test section up to ± 2 kPa, so the air velocity at the test section could be determined. An MPXA6115A pressure transducer was used for measuring ambient absolute pressure. The electronic speed controller used here was the Phoenix ICE HV 85 from Castle Creation. This module supports a feature of limited data logging capability. The RPM of the motor was recorded and processed offline. The current and voltage were read through an on board power supply unit's ammeter and voltmeter. A thermocouple was used to measure the ambient temperature.

summarizes the instruments and their respective accuracy data supplied by the manufacturer. In the load cell accuracy column, the first is non-linearity, and the second one is the hysteresis. The dSPACE as shown in Figure 27 and Figure 28 were used as a data acquisition system for this experimental test.

Figure 26 Wind Tunnel Test Setup

Table 13 Instrument Accuracy

Instruments	Measured Quantity	Unit	Accuracy
Load Cell	Thrust	N	±0.5% FSO, ±0.5% FSO
Pressure Transducer	Dynamic Pressure, Ambient absolute Pressure	kPa	±0.28 ±1.5
Electronic Speed Controller Datalog	RPM	RPM	± 1
Thermocouple	Temperature	Celcius	±0.1% reading + 1°C
Power supply Ammeter	Current	Ampere	±0.6% +2 digit
Power supply Voltmeter	Voltage	Volt	±0.3% +2 digit

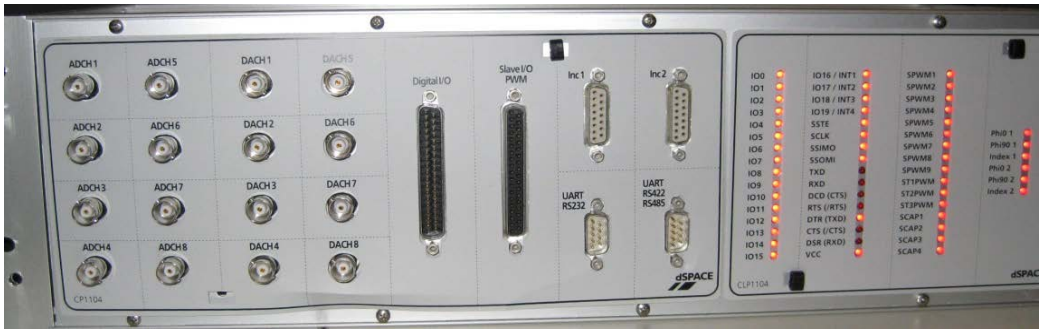

Figure 27 dSPACE CP1104 Connector Panel

Figure 28 dSPACE Controller Board

4.3.2 Error Analysis

The uncertainty analysis was conducted for all measured and calculated variables. For the measured variables the uncertainties were provided by the respective manufacturer of each instrument as shown in Table 13. This uncertainty for each measured variable was then used for determining the uncertainty of the calculated variable result defined by equation (69) based on the Kline-McClintok method explained in [24]. Equation (69) is as follows:

$$w_R = \left[\left(\frac{\partial R}{\partial x_1} w_1\right)^2 + \left(\frac{\partial R}{\partial x_2} w_2\right)^2 + \cdots + \left(\frac{\partial R}{\partial x_3} w_3\right)^2\right]^{0.5} \quad \textbf{(69)}$$

where R is the result, w_R is the uncertainty in the result, x_n are the dependent variables, and w_n are the associated uncertainty of those variables. This formula was used to calculate the uncertainty for the calculated variables in Table 15. The uncertainty was caused by the inherent uncertainty in the instrument used in the experiment.

4.3.3 Variables and Parameters

Table 14 shows the measured variables with their respective units. These variables were obtained directly from the instruments that were used. The calculated variables were required in order to evaluate the performance parameter. Table 15 summarizes the calculated variables and parameters.

Table 14 Measured Variables

Measured Quantity	Source	Variable	Unit
Thrust	Load cell	T	N
Dynamic Pressure	Presure transducer	q	kPa
Atmospheric pressure	Presure transducer	p	kPa
Revolution per Minute	Electronic Speed Controller	RPM	RPM
Temperature	Thermocouple	Tt	Celcius
Power Supply Current	Power Supply ammeter	Ips	Ampere
Power Supply Voltage	Power Supply voltmeter	Vps	Volt

Accounting for ideal gas conditions, the density of the air was calculated by the following relation,

$$\rho = \frac{p}{RT_t} \quad \textbf{(70)}$$

where the R is the specific gas constant for the dry air, 287.05 J/(kg.K), T_t is the temperature in kelvins, and p is the atmospheric pressure in pascals. The calculated density is important in order to calculate the other calculated variables and parameters dependent on density such as C_T, C_P, and advance ratio, J. However, C_P is difficult to calculate since it requires the propeller shaft torque measurement value and the experiment setup did not measure the torque of propeller shaft. Calculation of the uncorrected velocity is also important because the experimental results are a function of this variable. This can be calculated with the following relation shown in Table 15.

$$v = \sqrt{\frac{2q}{\rho}} \quad (71)$$

Table 15 Calculated Variables

Calculated Quantity	Variable	Unit
Air density	ρ	kg/m3
Air Velocity	v	m/s
Coefficient of Thrust	C_T	-
Coefficient of Thrust	C_P	-
Advance Ratio	J	-

4.3.4 Test Procedure

The validation test was conducted with the wind tunnel test section airspeed varied for three different airspeeds: 17.04, 19.43 and 23.46 m/s. For each, the wind tunnel corresponding supply voltage and current were determined based on the three optimization scenarios. All the tests were conducted at full throttle. Prior to recording the measurement data, the pressure transducer and the load cell were zeroed. Table 16 summarizes the experimental matrix used to conduct the experiments and presents their results.

Table 16 Experimental Matrix

Vpsu [V]	Ipsu [A]	V [m/s]	T [N]	RPM [RPM]	J	C_T	C_P
27.13	5.77	23.46					
28.265	4.215	19.43					
28.4143	4.02	17.04					

The performance variables of the propulsion system were recorded using dSPACE. The graphic user interface provided by dSPACE is used to display and manipulate any variable or parameter desired to be observed or recorded. Figure 29 shows a snapshot of an example of the dSPACE control desk layout.

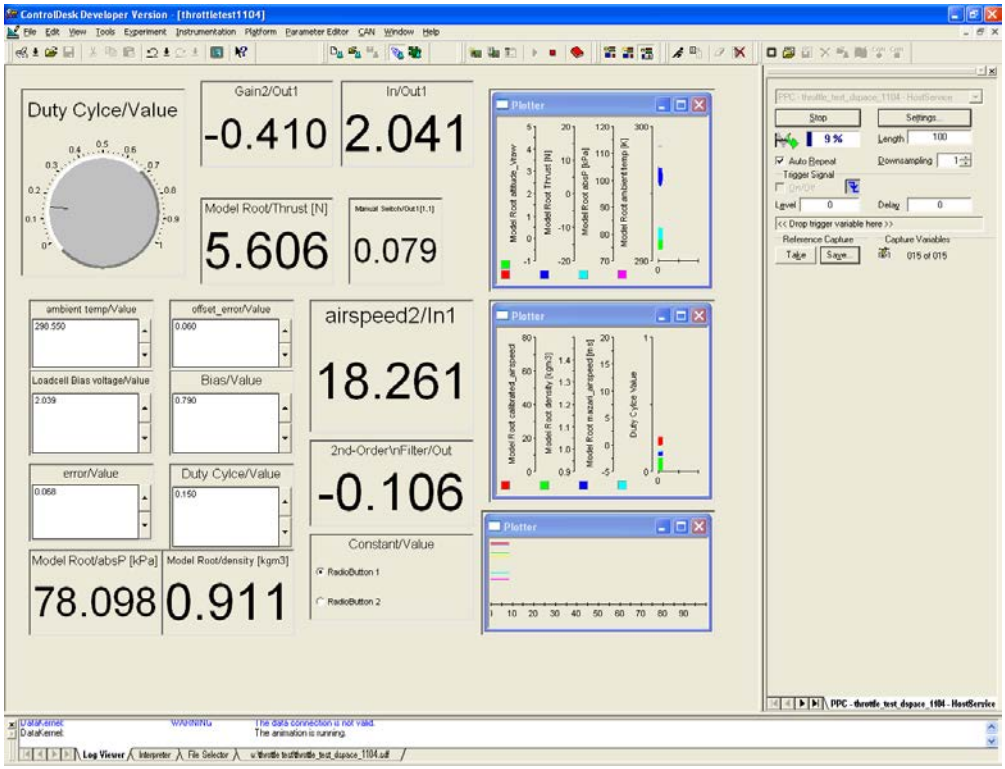

Figure 29 Control Desk Layout

4.4. Results and Discussion

4.4.2 Implementation of the Optimization

The results of the propulsion system optimization are presented in this section. Figure 30 to Figure 32 show the evolution history for each scenario that has been evaluated with regard to the objective function or fitness function maximizing the flight endurance. In the top graph of each figure, the blue dots show the mean value of the penalty function while the black dots are the best value at each generation.

The penalty function takes into account both the fitness function and the constraint violation [25]. The penalty functions select two design entities from the population for each generation and compare them for their consistency with the constraints and fitness function value. If the members are consistent with the constraint, then the penalty function value was set to be the fitness function value. Otherwise, the penalty value is the maximum fitness value among the worst feasible members of the population. The design entity with the minimum penalty value was selected for the subsequent generations. Hence, sometime during the intermediate generations there were members of the population that violated the constraints before the population converged to the best solution. As can be seen in Figure 30, the evolution process took many generations before the solution converged due to the low penalty value caused by constraint violation and positive or near positive fitness values.

As the evolution is marching forward, each new generation is converging toward the best penalty function value. This is due to the process of reproduction of the new generation being biased to the relation of the best penalty function value and the chance to be selected as parents of the new generation.

The optimization was stopped when any of the following criteria of termination were satisfied:

- The number of generations reaches the specified limit set by the user; in this case it is 100 generations. As can be seen in Figure 30 to Figure 32, in the stopping criteria plot, the generation is represented in terms of the percentage of the maximum generation.
- The optimization stop if the algorithm has been running for a certain amount of time in seconds which equals the specified limit; in this case it is infinite time.

- The stall (G) generations: the algorithm stops if the weighted average change in fitness function value over stall generation is less than the specified tolerance defined as 1e-6. The stall generation is 50 generations.
- The stall (T) time:if there is no improvement in the objective function or fitness function over an interval of time in seconds, the algorithm stops. The time interval is specified from the time limit value.

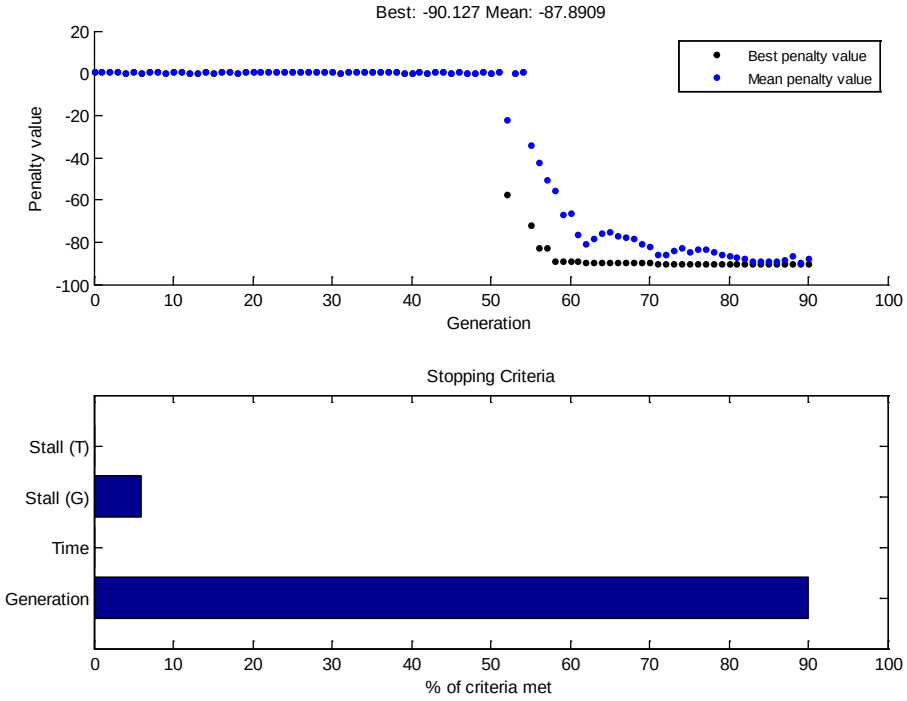

Figure 30 Evolution History of The Optimization for 1st Scenario (α = 0°)

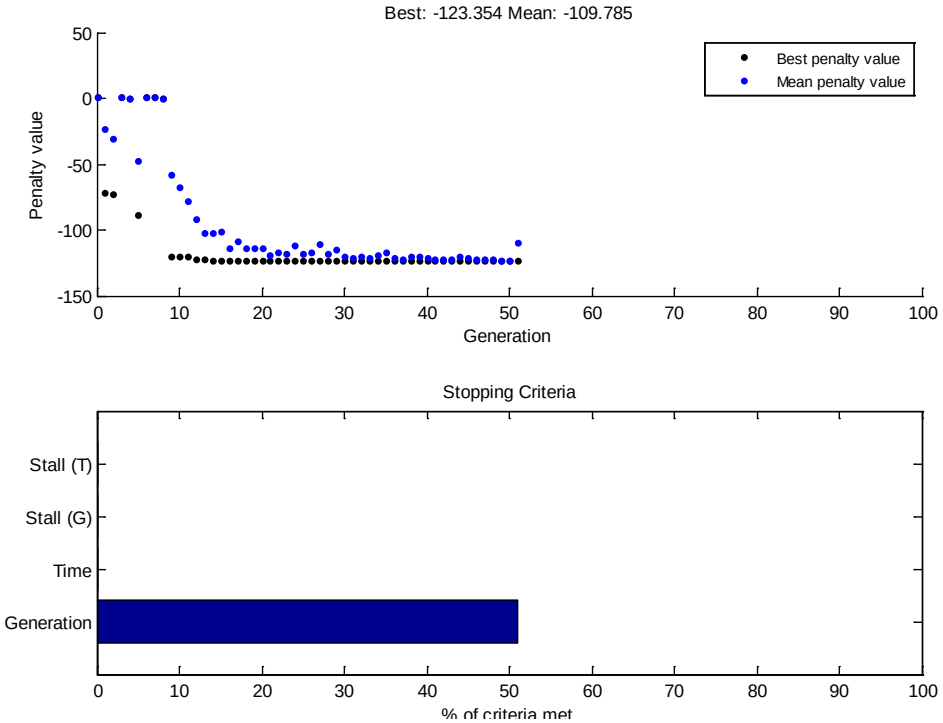

Figure 31 Evolution History of The Optimization for 2nd Scenario (α = 2°)

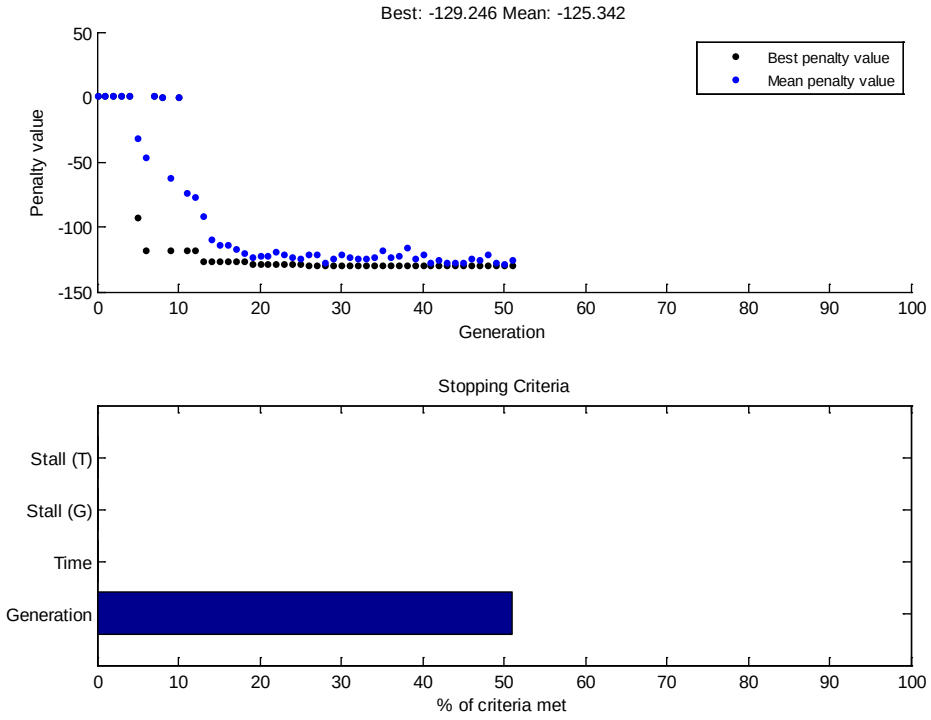

Figure 32 Evolution History of The Optimization for 3rd Scenario (α = 4°)

The results obtained from those three scenarios are presented in Table 17. As can be seen, the solutions for the three scenarios result in different propeller sizes used with the same motor and gear ratio. The 20 by 14 inch propeller offers longer

endurance but at slower speeds because the power required is a function of the cubic velocity. The propeller size is bigger than for the first two scenarios because it can produce more thrust at slower speeds. However, the solution for the third scenario only improves a little from the second scenario results. This is because the values of fuel cell current for both scenario are close in value (4 and 4.2 amperes). As outlined in section 3.6, the hydrogen consumption is a function of the fuel cell current.

Table 17 Summary of Optimization Results for All Scenarios

Scenario	AoA [deg]	Airspeed [m/s]	Propeller size [inch]	Motor Index	Gear Ratio	Endurance [min]	Range [m]	Power [W]
1	0	23.46	16 x 11	3	1	90	126684	156.5
2	2	19.43	17 x 12	3	1	123	143390	119.2
3	4	17.04	20 x 14	3	1	129	131580	114.3

The fitness value is the maximum endurance. The best endurance was obtained in the third scenario since the aircraft is made to fly at a 4 degree angle of attack where ${C_L}^{3/2}/C_D$ is at its maximum. The best range is obtained in the second scenario since the aircraft is made to fly at a 2 degree angle of attack where C_L/C_D is at its maximum as stated earlier in section 3.7. The hydrogen was stored in a 1.1 L tank at a pressure of 150 bars. So the endurance can be improved by carrying more hydrogen.

In all scenarios the motor and gear ratio was selected through optimization motor index 3 and gear ratio 1. The motor in the solution space is the motor with the lowest Kv in the list and the least weight compared to A60 18L or A60 16L. Motors with low Kv produce lower RPM at the same voltage. However, this kind of motor produces higher torque compared with the motor which has higher Kv. Thus, for producing the same amount of thrust, the lower Kv motor requires a bigger propeller in order to compensate for the low rotational speed. Equation (32) shows that the thrust produced is influenced by the diameter of propeller to the fourth power compared to the square of the rotational speed.

In equation (52) the hydrogen flow rate is a function of the fuel cell current, I_{fc}. Therefore, the solution which requires less fuel cell current, I_{fc}, for maintaining the flight has longer endurance. Table 18 describes the detailed performance parameter obtained from the optimization for the selected design.

Table 18 Performance Parameter of The Selected Design

Performance Parameter	Scenario 1	Scenario 2	Scenario 3	Unit
Fuel cell current, I_{fc}	5.7686	4.2147	4.0226	Ampere
Voltage current, V_{fc}	27.1299	28.2649	28.4143	Voltage
Propeller coefficient of Thrust, C_T	0.0222	0.0252	0.0252	-
Propeller coefficient of Power, C_P	0.0206	0.0234	0.0232	-
Coefficient of Lift, C_L	0.3331	0.4880	0.6429	-
Coefficient of Drag, C_D	0.0156	0.0201	0.0285	-
Cruise airspeed, v_{cruise}	23.4676	19.4310	17.0398	m/s
Drag Force, D	4.7062	4.1580	4.5174	N
Propeller speed, ω	502.3170	393.0568	295.8247	Rad/s
Advance ratio, J	0.7223	0.7193	0.7124	-
Propeller torque, Q_p	0.2825	0.2660	0.3368	Nm
Motor total torque, $Q_{m\ total}$	0.3780	0.3615	0.4323	Nm
Motor power, $P_{m\ total}$	156.5002	119.1286	114.2991	Watts
Fuel Cell power, P_{fc}	156.5002	119.1286	114.2991	Watts
Propeller power, P_p	141.8984	104.5455	99.6354	Watts
Motor efficiency, η_m	0.9067	0.8776	0.8717	-
Propeller efficiency, η_p	0.7783	0.7728	0.7726	-
Hydrogen molar rate, $\dot{N_{H2}}$	4.4313	3.2377	3.0901	Mols/hour
Endurance, t	90.1271	123.3542	129.2458	minutes

4.4.3 Experiment Results

The outcomes from the experiment were used to validate the results of the implementation of optimization. Thus any discrepancy that was found in the process could be used as a measure of the uncertainty of the multi-disciplinary analysis. As outlined in section 4.3.3, the propulsion setup was tested for three conditions and three different propeller setups for each condition.

4.4.3.1. Propeller size 16 by 11

The following section summarizes the measured variables obtained for propellers having a 16 inch diameter and an 11 inch pitch, and shown in Figure 33 to Figure 50. The data captured are noisy while the value represented in Table 19 are the average values of the obtained data.

Table 19 Measured Variables for Setup with 16" X 11" Propeller

Variable	Result	Unit
T	4.583	N
q	0.3585	kPa
p	102.685	kPa
RPM	3105	RPM
ω	325.218	Rad/s
Tt	297.5	Kelvin
Ips	5.73	Ampere
Vps	27.4	Volt

Based on the measured variables in Table 19 the calculated variables were obtained and are presented in Table 20. The measure of uncertainty of each calculated variable presented here was obtained by using the accuracy value provided in and implemented using equation (69) in section 4.3.1.

Table 20 Calculated Variables for Setup with 16" x 11" Propeller

Variable	Result	Unit
ρ	1.2024 ±0.0451	kg/m^3
v	24.4181 ± 3.44	m/s
C_T	0.0522 ± 0.01155	-
C_P	0.0027 ± 3.562E-05	-
J	1.1608 ± 0.1634	-

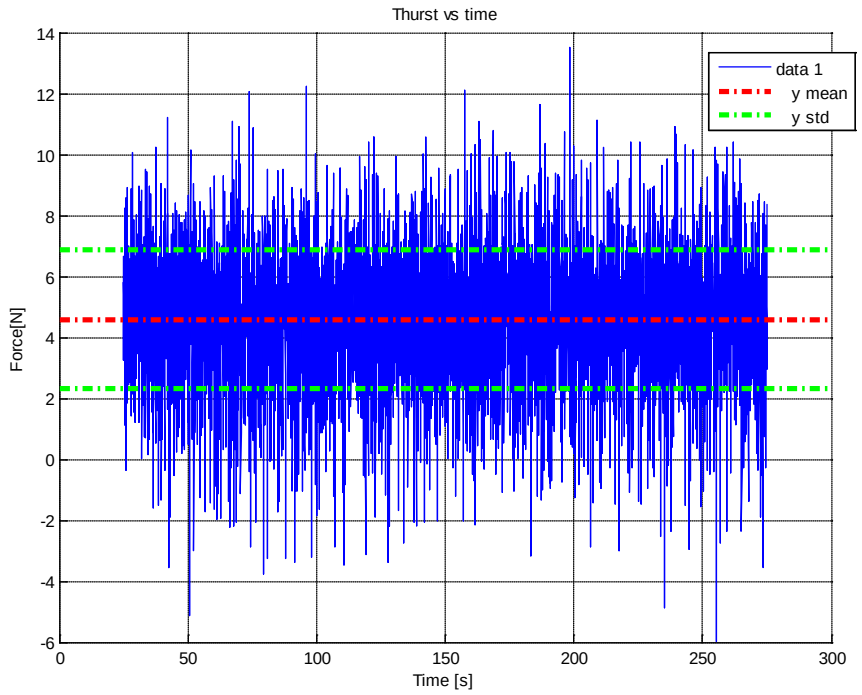

Figure 33 Thrust Measurement Data for Setup with 16" x 11" Propeller

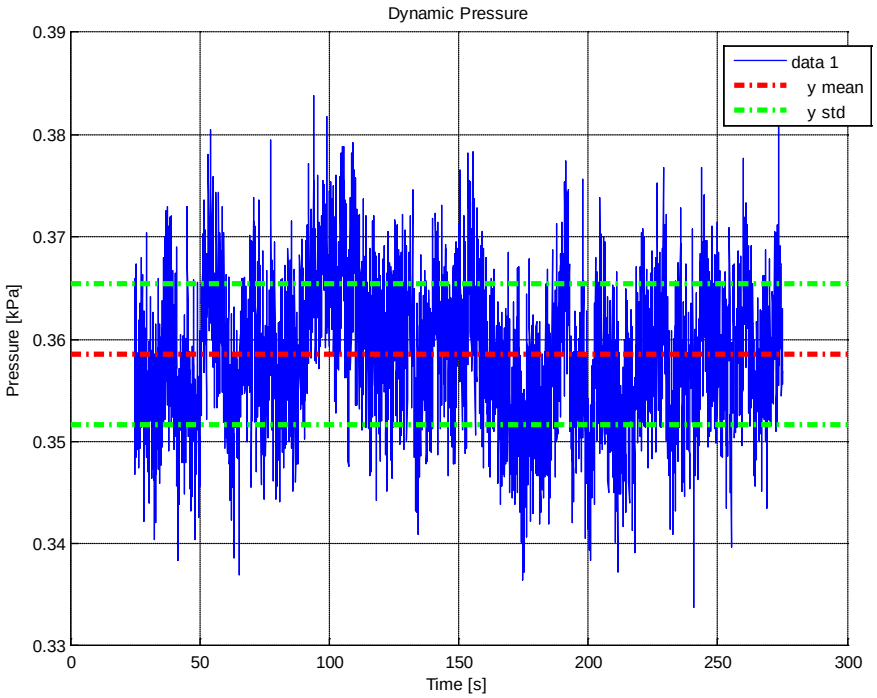

Figure 34 Dynamic Pressure Measurement at Airspeed 24.4 m/s

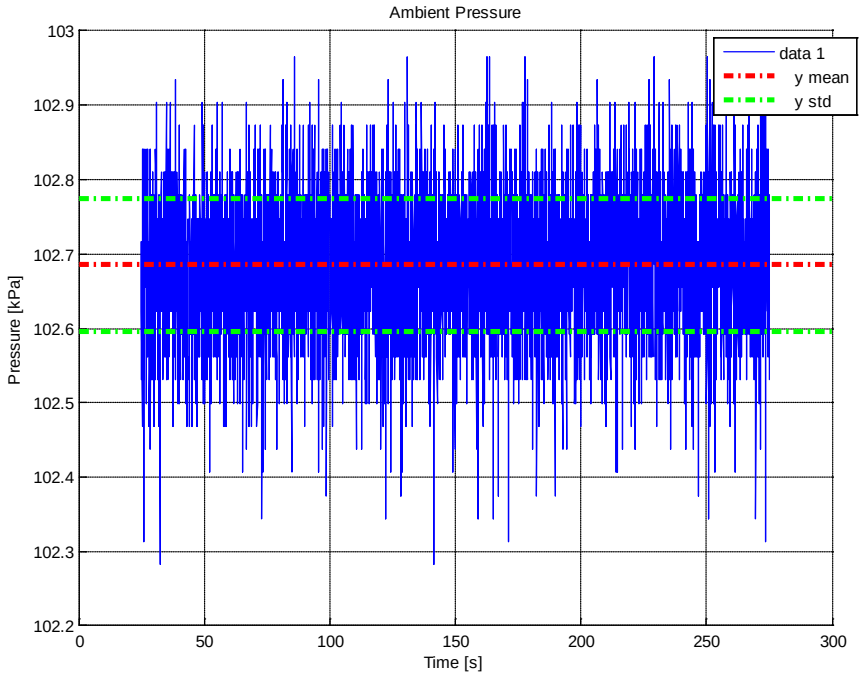

Figure 35 Ambient Pressure Measurement in The Respective Experiment

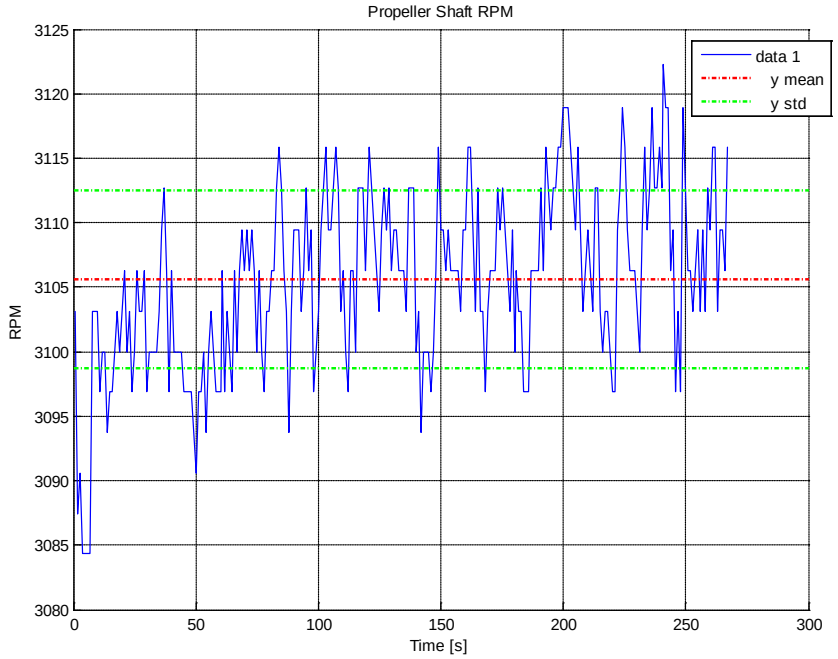

Figure 36 Propeller Shaft RPM Measurement for Setup with 16" x 11" Propeller

The rest of the results for 17 by 10 inch and 20 by 13 inch propeller are presented in the same manner subsequently. The discussions about the results are presented in section 4.4.3.

4.4.3.2. Propeller size 17 by 10

Table 21 Measured Variables for Setup with 17" X 10" Propeller

Variable	Result	Unit
T	3.8148	N
q	0.2458	kPa
p	102.6681	kPa
RPM	2915	RPM
ω	305.25	Rad/s
Tt	297.5	Kelvin
Ips	4.2	Ampere
Vps	28.2	Volt

Table 22 Calculated variables for setup with 17" x 10" propeller

Variable	Result	Unit
ρ	1.2022 ±0.0451	kg/m^3
v	20.219 ± 4.13	m/s
C_T	0.0387 ± 0.01024	-
C_P	0.0036 ± 2.191E-05	-
J	0.9638 ± 0.197	-

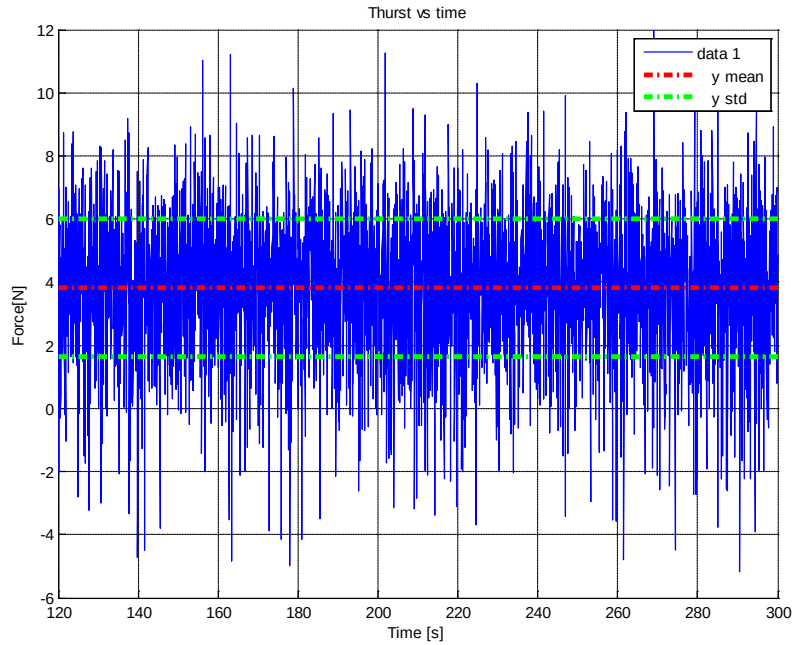

Figure 37 Thrust Measurement Data for Setup with 17" x 10" Propeller

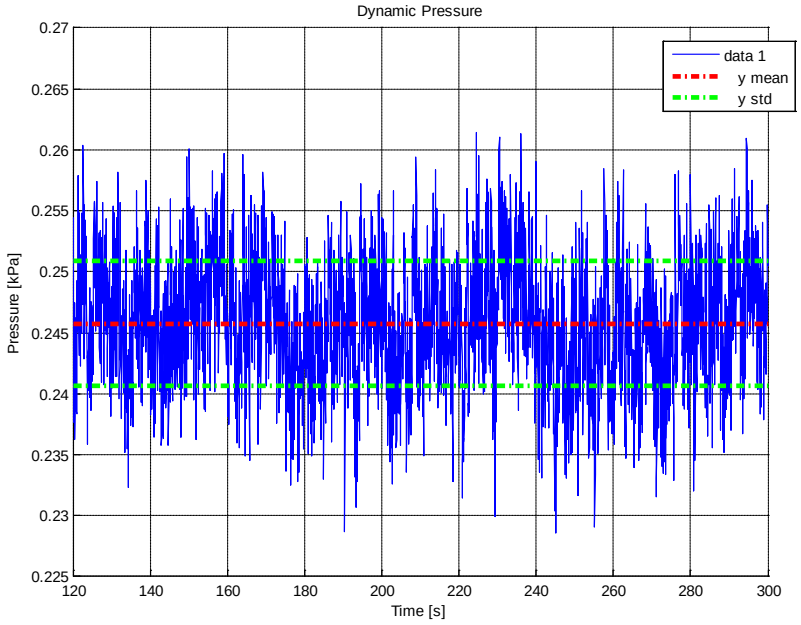

Figure 38 Dynamic Pressure Measurement at Airspeed 20.2 m/s

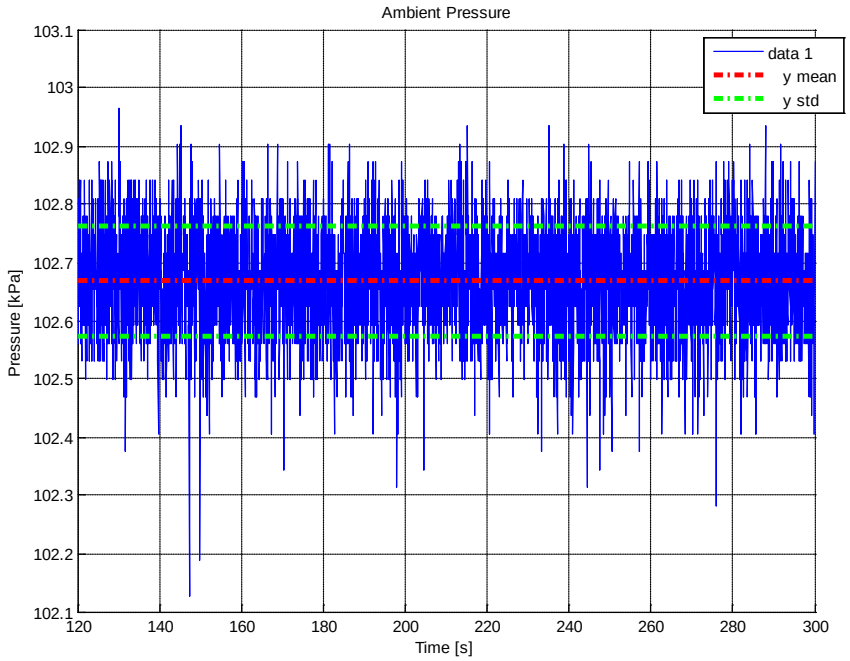

Figure 39 Ambient Pressure Measurement in The Respective Experiment

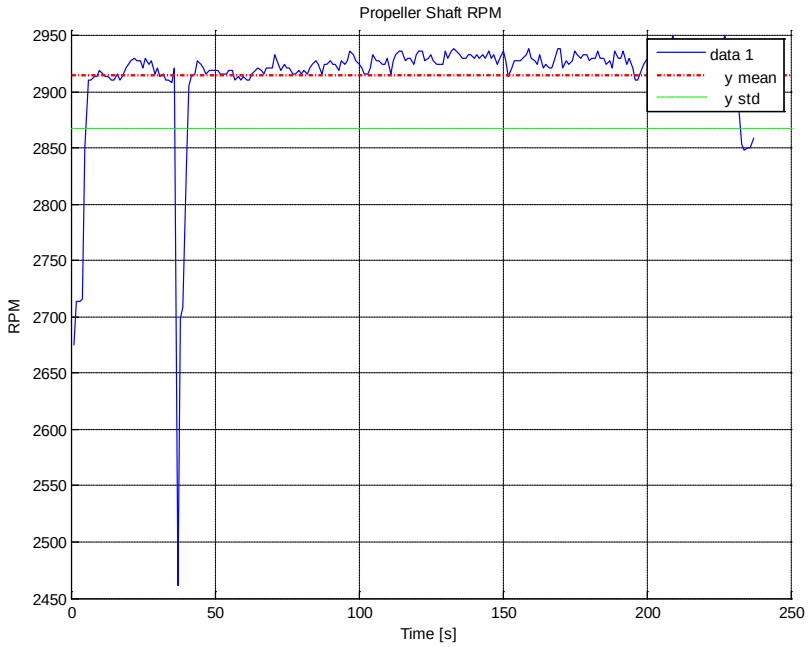

Figure 40 Propeller Shaft RPM Measurement for Setup with 17” x 10” Propeller

4.4.3.3. Propeller size 20 by 13

Table 23 Measured Variables for Setup with 20" X 13" Propeller

Variable	Result	Unit
T	5.615	N
q	0.1935	kPa
p	102.5297	kPa
RPM	2050	RPM
ω	214.69	Rad/s
Tt	298.55	Kelvin
Ips	4.03	Ampere
Vps	27.15	Volt

Table 24 Calculated Variables for Setup with 20" X 13" Propeller

Variable	Result	Unit
ρ	1.1964 ± 0.0448	kg/m^3
v	17.9848 ±4.66	m/s
C_T	0.0608 ± 0.010985	-
C_P	0.0031 ± 1.91E-05	-
J	1.0361 ± 0.27	-

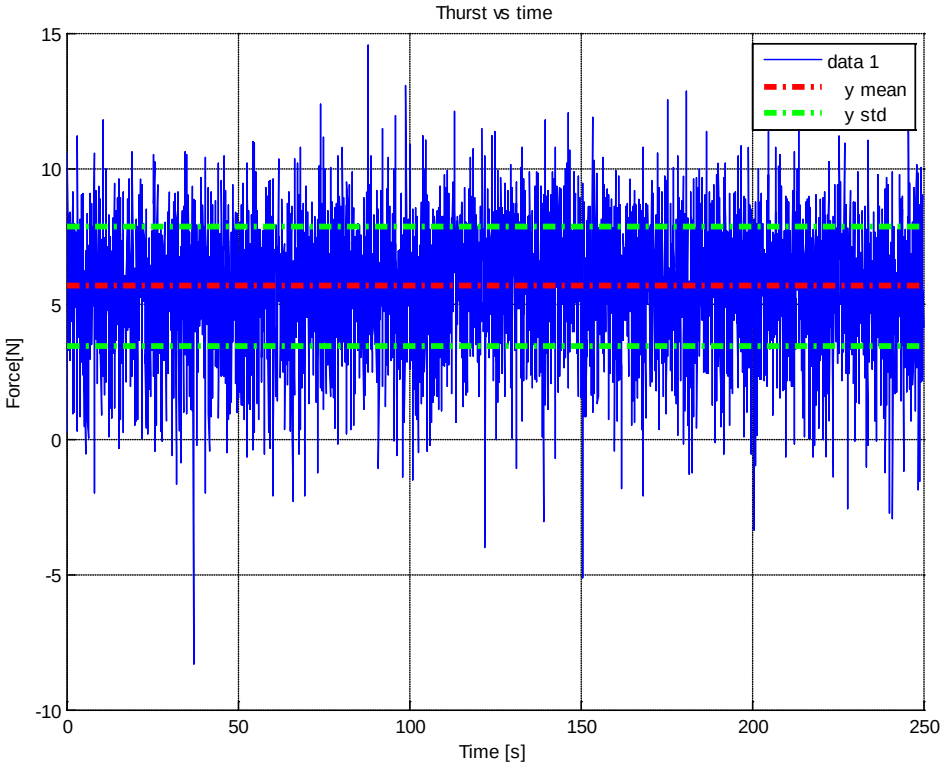

Figure 41 Thrust Measurement Data for Setup with 20" x 13" Propeller

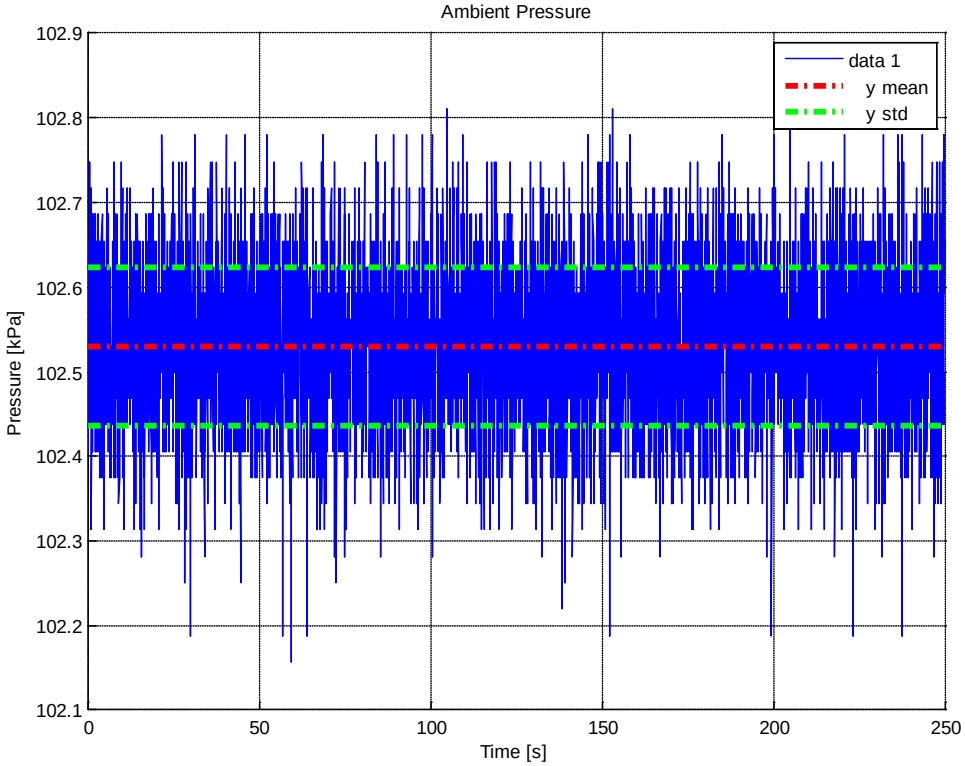

Figure 42 Ambient Pressure Measurement in The Respective Experiment

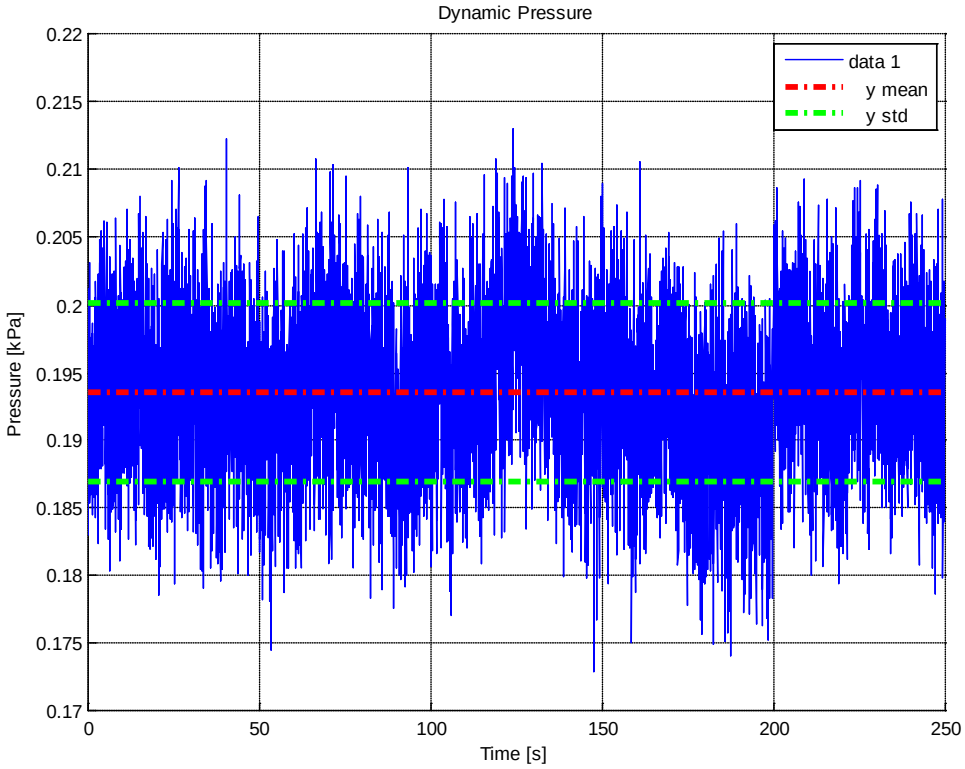

Figure 43 Dynamic Pressure Measurement at Airspeed 17.98 m/s

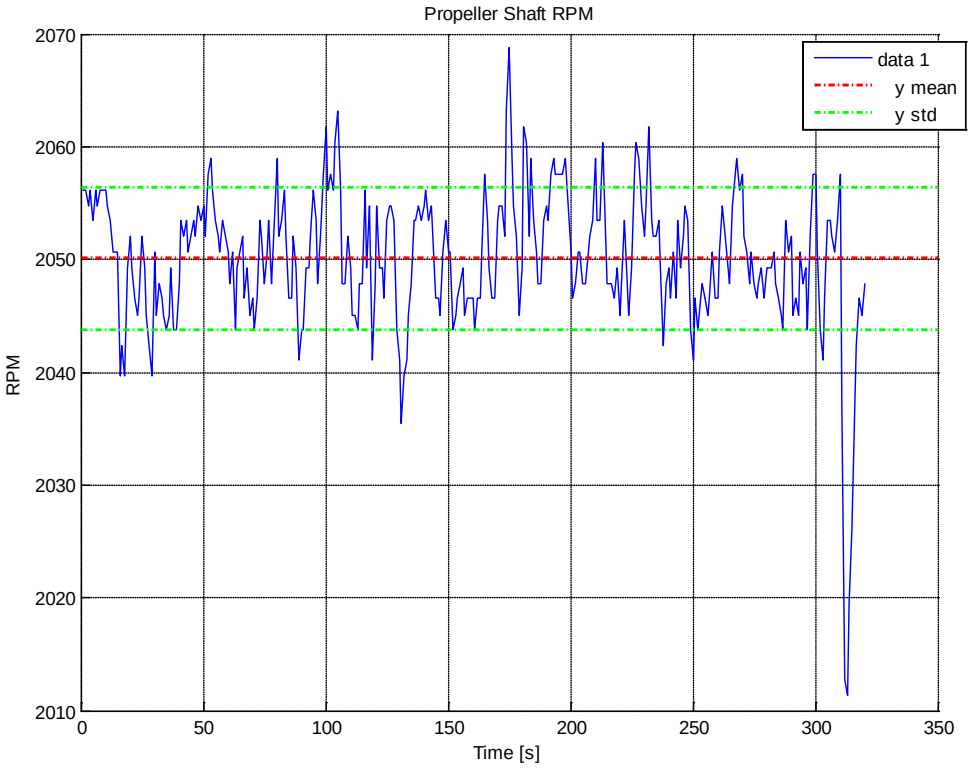

Figure 44 Propeller Shaft RPM Measurement for Setup with 20” x 13” Propeller

Table 25 summarizes the results obtained from the experiment and compares them with the optimization result.

Table 25 Experiment Results Compared with The Optimization

Parameter	16 x 11			17 x 10			20 x 13		
	Optimization	Experiment	Δ %	Optimization	Experiment	Δ %	Optimization	Experiment	Δ %
Voltage psu, V	27.130	27.400	1.00	28.265	28.200	0.23	28.414	27.150	4.4
Current psu,A	5.769	5.730	0.67	4.215	4.200	0.35	4.023	4.030	0.2
Airspeed, m/s	23.468	24.418	4.05	19.431	20.219	4.06	17.040	17.985	5.5
Variables									
Thrust, N	4.7062	4.583	2.62	4.158	3.8148	8.25	4.5174	5.615	24.3
ω, rad/s	502.317	325.28	35.24	393.0568	305.25	22.34	295.825	214.69	27.4
J	0.7223	1.1608	60.71	0.7193	0.9638	33.99	0.7124	1.0361	45.4
CT	0.0222	0.0522	135.14	0.0252	0.0387	53.57	0.0252	0.0608	141.3
CP	0.0206	0.0027	86.89	0.0234	0.0036	84.62	0.0232	0.0031	86.6
Power	110.44	111.91	10.60	80.79	77.13	33.47	76.98	100.99	134.78

4.4.4 Classical Approach Results

This section presents the classical approach for the motor and propeller selection process including the outcome of the endurance of the flight. Since the fuel cell power output was 200W, the power for cruising was expected to be less than 200W. Therefore, the selection of the motor and propeller was based on this limitation. The motor and propeller should produce adequate thrust to propel the airplane to overcome the drag and maintain the flight at cruising speed while consuming less than 200W of power. Reference [26] explains the details of this approach.

From the aerodynamics analysis it is known that the thrust requirement for the cruise flight is described in Table 26:

Table 26 Thrust Required for Three Cruise Conditions

AoA	Vcruise	Thrust	Power
0	17.1	4.673631	79.91909
2	19.4	4.188341	81.25381
4	23.5	4.500758	105.7678

Four propellers were considered and the performance characteristics are given in Table 27 obtained from [5]. For the cruise speed of 19 m/s, the following thrust performance plot (Figure 45) was generated based on Table 27 and using equation (32). The motors considered here are presented in. The motors shown in Table 28 have a Kv ranging from 149 to 600 RPM/V. All selected motors are Hacker™ motors.

Table 27 Propeller Performance Characteristics

Propeller	Coefficients
APC 22xl2	$C_T = -0.039J^2 - 0.055J + 0.062$ $C_P = -0.049J^2 - 0.001J + 0.031$
APC 24xl2	$C_T = -0.038J^2 - 0.055J + 0.057$ $C_P = -0.045J^2 - 0.005J + 0.028$
APC 26xl5	$C_T = -0.040J^2 - 0.053J + 0.067$ $C_P = -0.053J^2 - 0.002J + 0.042$
APC 27x13	$C_T = -0.037J^2 - 0.055J + 0.054$ $C_P = -0.044J^2 - 0.005J + 0.026$

Table 28 Motor Specification Data

No	Motor	Kv		R	I0
		[rpm/v]	[rad/s/volt]	[ohm]	[ampere]
1	A60 18L	149	15.6033	0.016	1.6
2	A60 24S	200	20.944	0.038	1.3
3	A50 16S	380	39.794	0.026	2
4	A40 10L	600	62.832	0.018	2.4

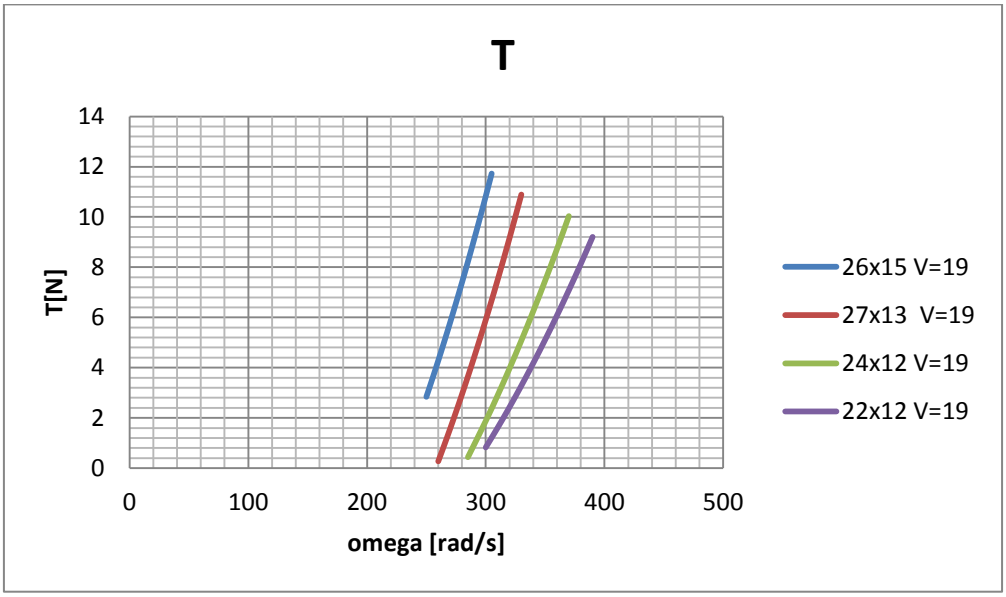

Figure 45 Propeller's thrust Performance at Airspeed 19 m/s

Based on the chart in Figure 45, the 26 by 15 inch propeller has the advantage of a steeper slope. This means it is more sensitive to the change in shaft rotational speed. Therefore it can produce a larger thrust for a given propeller in the chart at a lower rotational speed.

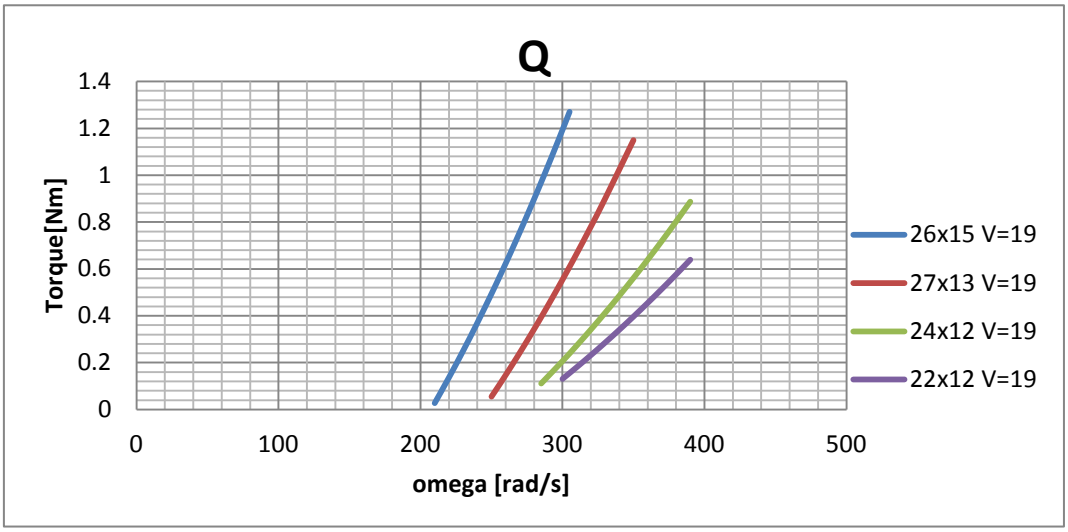

Figure 46 Propeller Torque Performance at Airspeed 19 m/s

By examining the toque chart in Figure 46, we can find the torque produced by the propeller at corresponding rotational speeds of the propeller. In Table 29 the torque and power produced for 5 N thrust of every propeller are presented as well as the voltages for each motor. All of the propellers consume less than 200 W of power to produce 5 N thrust. The selection is not straight forward; therefore one needs to look at to the motor performance as well to conclude the selection.

Table 29 Propeller Torques and Motor Voltages at Thrust 5 N and Airspeed 19 m/s

T = 5 N @ V=19 m/s				Motor Voltages			
propeller	Ω [rad/s]	Q [Nm]	P [Watts]	A60 18L	A60 24S	A50 16S	A40 10L
26x15	265	0.558017	147.8746	17.14856	13.14633	7.28872	4.891909
27x13	295	0.499782	147.4357	19.0567	14.53237	7.98236	5.303511
24x12	330	0.41246	136.1118	21.27802	16.134	8.771554	5.761794
22x12	350	0.396672	138.8353	22.55586	17.07637	9.257814	6.062249

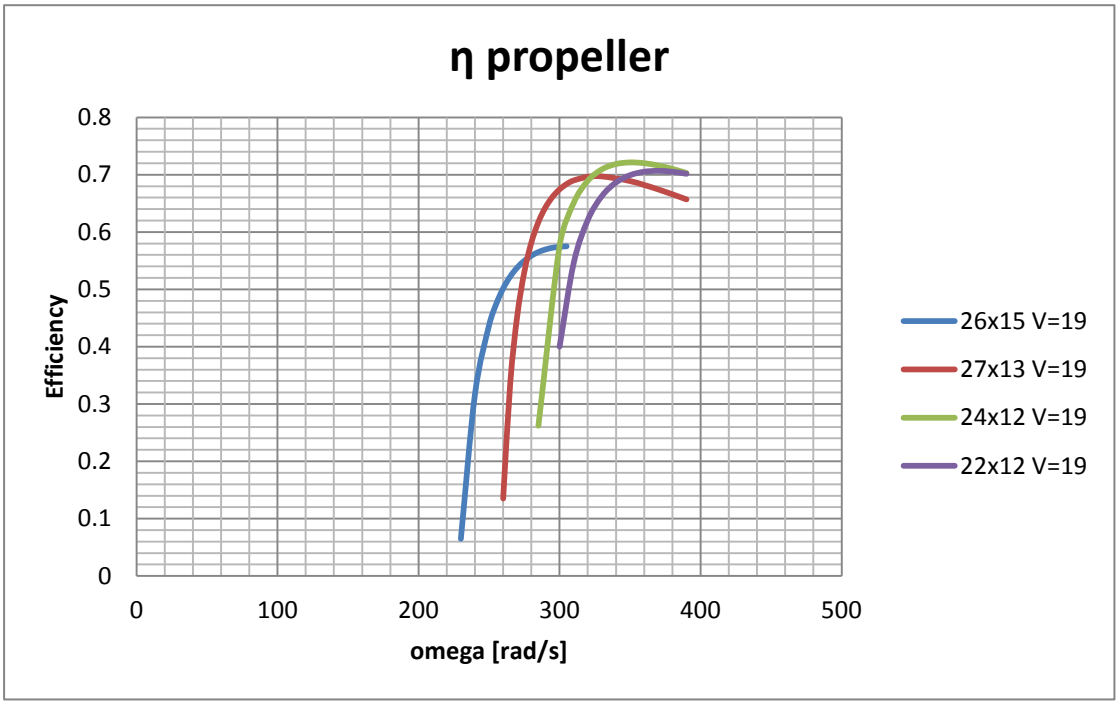

Figure 47 Propeller Efficiencies Chart

Considering that the power consumption and the efficiency are critical for the endurance flight, the 24 x 12 inch propeller was selected. This is due to its efficiency and its power output being the least among the four candidates. To select the appropriate motor for this propeller, according to reference [26] the motor and propeller should be matched based on their efficiency curve. Both have to have their efficiency peaks roughly at the same rotational speed. Figure 48 shows the efficiency

curves for each motor when subjected to the voltage required to run the propeller for producing 5 N thrust using a 24 by 12 inch propeller.

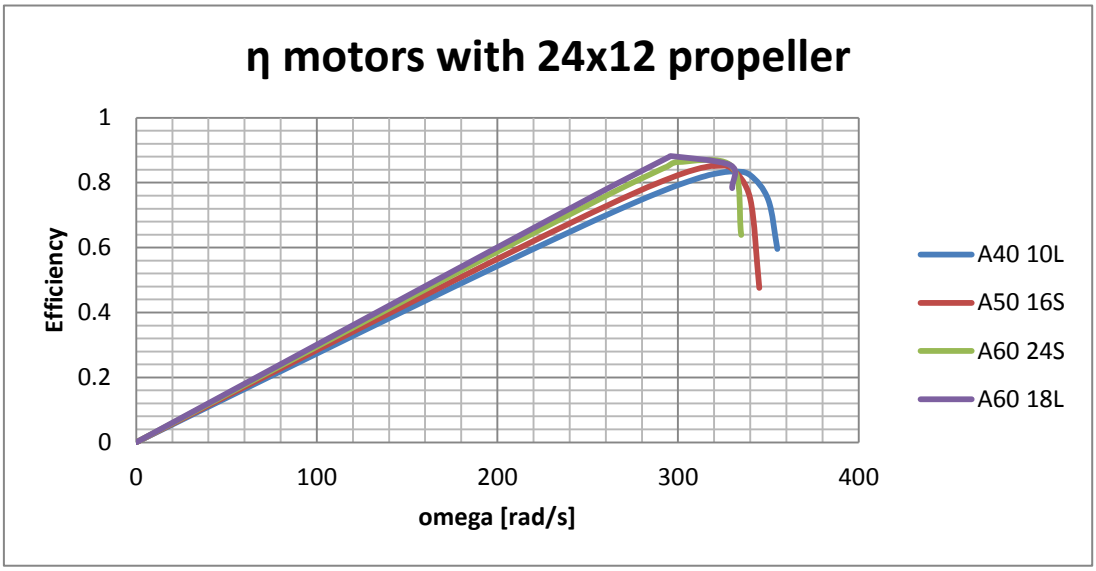

Figure 48 Motors Efficiencies for 24 by 12 inch Propeller

As shown in Figure 48, all the motors roughly have peaks at speeds of 300 to 330 rad/s. Therefore, to decide the final propeller size we need to look into the motor's recommended propeller size and see what is the maximum propeller size that can be attached for each motor. This step is also used to avoid overloading the motor as shown in Table 30.

Table 30 Recommended Propeller Size

No	Motor	Recommended Prop size
1	A60 18L	24x12
2	A60 24S	20x13
3	A50 16S	17x9
4	A40 10L	9x6

Based on this consideration it was decided that the best motor is the A60 18L with a 24 by 12 inch propeller. Table 31 shows the performance of this propulsion configuration when paired with the fuel cell and used to propel the same aircraft. For all scenarios the propeller and motor pair is the same.

Table 31 Performance Parameter of The Selected Design

Performance Parameter	**Scenario 1**	**Scenario 2**	**Scenario 3**	**Unit**
Fuel cell current, I_{fc}	7.3986	4.9952	4.4913	Ampere
Voltage current, V_{fc}	26.0793	27.6785	28.0533	Voltage
Propeller coefficient of Thrust, C_T	0.0075	0.0091	0.0118	-
Propeller coefficient of Power, C_P	0.0071	0.0081	0.0097	-
Coefficient of Lift, C_L	0.3331	0.488	0.6429	-
Coefficient of Drag, C_D	0.0156	0.0201	0.0285	-
Cruise airspeed, v_{cruise}	24.0094	19.8361	17.282	m/s
Drag Force, D	4.926	4.3332	4.6467	N
Propeller speed, ω	394.009	334.189	304.385	Rad/s
Advance ratio, J	0.6281	0.6118	0.5852	-
Propeller torque, Q_p	0.455	0.3729	0.3692	Nm
Motor total torque, $Q_{m\,total}$	0.5576	0.4755	0.4717	Nm
Motor power, $P_{m\,total}$	192.95	138.259	125.996	Watts
Fuel Cell power, P_{fc}	192.95	138.259	125.996	Watts
Propeller power, P_p	179.283	124.633	112.371	Watts
Motor efficiency, η_m	0.9292	0.9014	0.8919	-
Propeller efficiency, η_p	0.6597	0.6896	0.7146	-
Hydrogen molar rate, $\dot{N_{H2}}$	5.6835	3.8372	3.4502	Mols/hour
Endurance, t	70.2705	104.081	115.758	minutes

4.4.5 Discussion

Table 25 shows the comparison between the results obtained from the optimization algorithm and those obtained from the experiment. The largest error in parameter is only 5.5% which is considered acceptable. However, for the variables, the results show various levels of discrepancy between the optimization and experimental validation. The least error is in the thrust for all setups, while the most significant error is in the coefficient of thrust. In equation (32), the discrepancy that occurred significantly for C_T has two main contributors: the thrust, T, and the rotational speed, ω; the air density and propeller diameter are the same for all setups. The rotational speed, ω, compared with thrust contributes more to the discrepancy due to the fact that it is squared power. Thus, even for a small discrepancy in the rotational speed, ω manifested significantly in the coefficient of thrust discrepancy.

$$C_T = \frac{T}{\rho(\omega/2\pi)^2 {d_p}^4} \tag{72}$$

The propulsion setup used in the experiment is not the same as the one proposed by the design optimization. Even though the motor specification K_V is close to those used in the optimization, the no load current and the resistance can be different and of course produce different speeds as can be seen in the Table 32. Moreover, for configurations with a gear ratio equal to one, at the steady state condition, the propeller torque and the motor shaft torque are equal. The magnitude of the torque required by the propeller to run at a steady state condition also contributed to the propeller rotational speed. Hence, the motor will draw any necessary current to compensate for any difference in torque until reaches the steady state condition in torque. Therefore, the rotational speed required for each propeller size and type to produce a certain amount of thrust is different. Since the rotational speed is less than that in the optimization, the advance ratio in the experiment result is higher.

Table 32 Motor Specifications of Hacker A60 20M and C50 15XL with Gearbox

Motor Name	Kv [RPM/V]	I0 [A]	Rm [Ohm]	V0 [Volts]
A60 20M	170	1.7	0.032	8.4
C50 15XL with gearbox	173.13	1.2	0.028	8.4

Even though the first setup used the same propeller size, for both the experiment and optimization the result of the coefficient of thrust is very different.

This is due to the type of propeller that was used since it is made for an internal combustion engine instead of an electric motor. The experiment was conducted by using the available propeller and motor setup for which the specification was close to the optimization result. There is a difference in the plan form of the two types of propellers depicted in Figure 49. The distribution of the cord length of the propeller blade is also different for both types. This distribution determines the distribution of the thrust load along the blade and thus the total thrust can be different for both at the same operating condition. Hence, the coefficient of thrust of both can be different as well for the same operating condition although the specification is the same. This also happened for the coefficient of power, $C_{P.}$ However, the result of C_P in the experiment is only an estimate using the relation in equation (39) based on the current supplied since the test setup did not measure the torque of the propeller shaft.

Figure 49 Electric Propeller at the bottom and Combustion Engine Propeller at the top

From the experimental results presented in the previous section it can be seen that the reading from the dynamic pressure (which also represents the airspeed in the test section) and the thrust reading were fluctuating. The deviation of the dynamic pressure resulted in deviation of the airspeed in the test section. The fluctuation of the airspeed on average is less than 1 m/s as can be seen in Figure 50 below which considered acceptable.

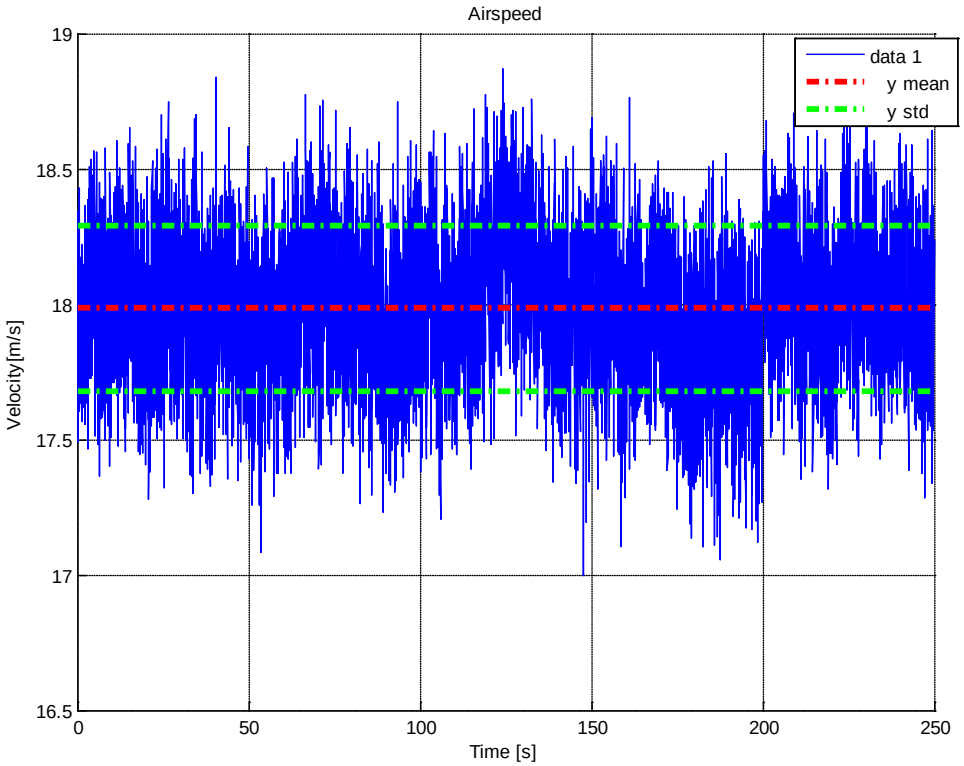

Figure 50 Airspeed Measurement with Setup 20" x 13" Propeller

The thrust measurement (summarized in Figure 33, Figure 37 and Figure 41) shows significant fluctuations compared to its mean value. In some events the readings went to negative value. This means the load cell was experiencing compression for very short time. The mounting plate therefore was vibrating in a longitudinal direction where the motion was not constrained. This problem appeared in each thrust measurement. One factor causing vibration of the stand is the effect from the air stream produced by the propeller impacting the mounting plate which creates air wakes around it and vortex shedding.

Table 33 shows the classical approach results showing the same trends as the optimization approach results. The 3rd scenario gives the best endurance among all because of the ratio $\left({C_L}^{3/2}/C_D\right)_{max}$. However, if the classical approach were used to evaluate the same range of motors, propellers and gear ratios as were implemented in the optimization, the process would require many chart plottings of thrust, torque and efficiencies of motor and propellers for different operating points. The endurances found from the classical approach were less than those obtained by design optimization. This is due to the limited number of propellers and motors that were evaluated. So the optimization approach using a genetic algorithm can help in finding

a global solution and avoiding the tedious effort involved in comparing and examining the performance chart of propellers and motors.

Table 33 Comparison of Classical Approach and Optimization on Endurance Parameter

Endurance	Scenario 1	Scenario 2	Scenario 3	Unit
Classical Approach	70.2705	104.081	115.758	minutes
Optimization using GA	90.1271	123.3542	129.2458	minutes
Increment %	28.2574	18.5175	11.6517	

5. Conclusion and Future Work

5.1. Summary and Conclusion

The objective of this work was to develop a tool that optimizes the endurance of a fuel cell powered unmanned aerial vehicle. The selection of the electric propulsion system components is critical in order to achieve the desired flight performance of the UAV powered by a 200 watt PEM fuel cell. This design optimization approach of the electric propulsion system is constrained to components that are commercially available in the market. Commercially off the shelf (COTS) components are not designed for long endurance flights. This work provides a method to select and to find a motor, propeller, and gear ratio combination that will give the highest possible flight endurance for the given range of components powered by the fuel cell.

The optimization process involved the modeling, analysis and searching of each system component from COTS. The motor, propeller, fuel cell, and UAV were modeled. These models were used for simple flight endurance analysis. The genetic algorithm was successfully used as a searching method for matching the propeller, electric motor, and gear ratio with the limited power output from the fuel cell. The analysis of each model was solved simultaneously using the fsolve function. Most of the mathematical models were derived from its physic relation except for the fuel cell and the propeller model. The fuel cell polarization model was built based on empirical data obtained from the fuel cell stack. The propeller model consisted of an artificial neural network model that was trained based on the data provided by the manufacturer. Fuel cell and propeller models were chosen in order to achieve a good accuracy of propeller coefficient of thrust and power which are very important in estimating the thrust and power.

Experimental validation of the design optimization was conducted in the wind tunnel. Experimental setup was designed in order to investigate the validity of the multi-disciplinary analysis with the actual system performance. However, the test was only conducted using components which were already available in the lab. The test setup needed to be improved to get better and cleaner measurement readings. The mechanical design of the test setup needs to be changed in order to minimize the vibration and also provide a way to measure the thrust and the torque of the motor at the same time.

The solution found by the presented optimization process suggests using a low voltage constant electric motor with a large diameter propeller. The low Kv motor can produce higher torque at the same current as the higher Kv motor. This is due to the torque constant of the motor being inversely proportional with Kv. Since a low Kv motor produces lower rotational speed per volt, to produce the same thrust force it requires bigger propeller diameter and or bigger propeller pitch. The thrust requirement and propeller size govern the rotational speed of the propeller which should be delivered by the motor. The bigger diameter of the propeller requires less rotational speed than the smaller propeller size to produce the same amount of thrust. The tradeoff between propeller size, gear ratio, armature resistance, and motor rotational speed and its constant determines the current required for the motor to run at propeller required speed. The hydrogen consumption is dictated by the amount of current drawn from the fuel cell stack. In other words, the less current used to produce the required thrust means less hydrogen consumed and longer endurance. Using design optimization methodology, the exhaustive tradeoff for selecting propulsion system components can be avoided. When compared with the classical trial and error approach, design optimization results show significant improvement in endurance.

5.2. Future Work

The optimization can be extended by taking into account the aircraft design configuration parameters as the design variables, as well as covering the full flight profile of the aircraft. Moreover, the multi-disciplinary analysis can also include more accurate models of fuel cell systems. In addition, the fuel tank capacity can be included as the design variable so that the endurance can be extended by means of carrying more fuel. Apart from design and optimization, the continuation of this work also can be done in the implementation stage of flight testing and the improvement of the experimental test setup. The result of this optimization and the aircraft design can be realized by building an airframe integrated with the selected propulsion system followed by the flight test verification.

6. References

[1] B.A. Moffitt, T.H. Bradley, D. Mavris and P.E. David, "Design Space Exploration of Small-Scale PEM Fuel Cell Long Endurance Aircraft," *American Institute of Aeronautics and Astronautics.*

[2] T.H. Bradley, B.A. Moffitt, T.F. Fuller, D. Mavris and D.E. Parekh, "Design Studies for Hydrogen Fuel Cell Powered Unmanned Aerial Vehicles," *American Institute of Aeronautics and Astronautics.*

[3] B.A. Moffitt, T.H. Bradley, D.E. Parekh and D. Mavris, "Design and Performance Validation of a Fuel Cell Unmanned Aerial Vehicle," in *44th AIAA Aerospace Sciences Meeting and Exhibit,* 2006.

[4] C. Herwerth, U. Ofoma, D. C. Wu, S. Matsuyama and S. Clark, "Development of a Fuel Cell Powered UAV for Environmental Research," in *44th AIAA Aerospace Sciences Meeting and Exhibit*, Reno, Nevada, 2006.

[5] P. Lindahl, E. Moog and S.R. Shaw, "Simulation, Design and Validation of a UAV SOFC Propulsion System," in *IEEE Aerospace Conference*, 2009.

[6] C. Chiang, C. Herwerth, D. Mirmirani, A. Ko, S. Matsuyama, S.B. Choi, D. Gamble and D. Arena, "Systems integration of a hybrid PEM fuel cell/battery powered endurance UAV," in *46th AIAA Aerospace Sciences Meeting and Exhibit*, 2008.

[7] T.H. Bradley, B.A. Moffitt, D.E. Parekh, T.F. Fuller and D.N. Mavris, "Energy Management for Fuel Cell Powered Hybrid – Electric Aircraft," in *7th International Energy Conversion Engineering Conference*, 2009.

[8] G.D. Rhoads, N.A. Wagner, B.J. Taylor, D.B. Keen and D.T. H. Bradley, "Design & Flight Test Result for 24 Hour Fuel Cell Unmanned Aerial Vehicle," in *8th Annual International Energy Conversion Engineering Conference*, Nashville, 2010.

[9] N. Wagner, S. Boland, B. Taylor, D. Keen, J. Nelson and T. Bradley, "Powertrain Design for Hand-Launchable Long Endurance Unmanned Aerial Vehicles," *American Institute of Aeronautics and Astronautics,* 2010.

[10] D. Goldberg, Genetic Algorithms in Search, Optimization, and Machine Learning, Addison-Wesley, 1989.

[11] X.-P. Forum, "X-Plane.Org Forum," 2012. [Online]. Available: http://forums.x-plane.org/index.php?showtopic=41729. [Accessed 13 01 2013].

[12] H. Education Bureau, "Physics World," 2 2010. [Online]. Available: http://www.hk-phy.org/energy/transport/trans_is02_e.html. [Accessed 2012 12 7].

[13] C. Honsberg and S. Bowden, "PVCDROM," December 2010. [Online]. Available: http://pvcdrom.pveducation.org/BATTERY/Images/image023.gif. [Accessed 7 12 2012].

[14] W. F. Phillips, Mechanics of Flight, John Wiley, 2004.

[15] FuelCells.org, August 2012. [Online]. Available: http://www.fuelcells.org/. [Accessed 24 12 2010].

[16] A. Tools.com, "Airfoil Tools," 8 2012. [Online]. Available: http://airfoiltools.com/polar/details?polar=xf-sd7032-il-500000. [Accessed 1 12 2012].

[17] D. o. A. E. UIUC Applied Aerodynamics Group, "UIUC Airfoil Coordinates Database," 7 2012. [Online]. Available: http://www.ae.illinois.edu/m-selig/ads/coord_database.html. [Accessed 19 6 2010].

[18] L. Products, "Advanced APC propellers precision composites," 8 2012. [Online].Available: http://www.apcprop.com/v/downloads/PERFILES_WEB/datalist.asp. [Accessed 5 10 2012].

[19] D. Gorissen, I. Couckuyt, P. Demeester, T. Dhaene and K. Crombecq, "A Surrogate Modeling and Adaptive Sampling Toolbox for Computer Based Design," *Journal of Machine Learning Research,* vol. 11, 2010.

[20] Y. Zhu and K. Tomsovic, "Development of models for analyzing the load-following performance of microturbines and fuel cells," *Electric Power Systems Research,* vol. 62, pp. 1-11, 2002.

[21] H. E. systems, "Aeropak Fuel Cell Power System - Operation & Maintenance Guide Manual," Horizon Energy Systems, Singapore, 2012.

[22] G. J. Rujigrok, Elements of airplane performance, 2nd Edition ed., Delft: VSSD, 2009.

[23] A.-M. I. /. H. B. USA, "Aero-Model Incorporated," Aero-Model Incorporated, 2012. [Online]. Available: https://www.aero-model.com/aero-model/8_79_1057/Motors_Hacker%20C50%20Competition/C50-15XL-COMP%20MOTOR.html. [Accessed 5 12 2012].

[24] M. P. Merchant, "Propeller Performance Measurement for low reynolds number Unmanned Aerial Vehicle Applications," Wichita State University, Wichita, 2005.

[25] Mathworks, "Mathworks," 4 2012. [Online]. Available: http://www.mathworks.com/help/gads/mixed-integer-optimization.html?s_tid=doc_12b#bs1cihn.

[26] M. Drela, *Lab 5* Lecture *Notes - DC Motor / Propeller Matching,* MIT, 2005.

[27] F. Semiconductor, "Technical Data - Integrated Silicon Pressure Sensor On-Chip Signal Conditioned, Temperature Compensated and Calibrated MPXV7002 SERIES," Freescale Semiconductor, 2005.

[28] P. Carpenter, "RC Airplane World," 12 2012. [Online]. Available: http://www.rc-airplane-world.com/image-files/aerodynamic-forces.gif. [Accessed 7 12 2012].

7. Appendices

A. Fuel Cell UAV Design Summary

The following tables show a summary of the UAV configuration and specifications:

4.4.6 A.1 Initial Sizing

Since the weight, wing area, cruising speed and the CL design were already determined in the previous section, those data can be used as the starting point for the design. The following table summarizes the starting design point of the aircraft.

Table 34 Initial Design Point

Initial Design Point					
Weight	6.8	Kg	ρ	1.2133	Kg/m^3
Wing Area	0.9	m^2	g	9.81	m^2/s^2
W/S	7.55	Kg/m^2	viscosity	1.78E-05	m^2/s
CL_{design}	0.4		Cruise Speed	19	m/s
			Cruise Altitude	100	m

4.4.7 A.2 Wing Sizing

See Table 5 in section 3.1.

4.4.8 A.3 Tail Sizing

With the conventional aircraft configuration, the aircraft has one vertical tail plane (VTP) and one horizontal tail plane (HTP). The sizes for both of them are determined by choosing the typical historical statistics data of the existing aircrafts. The relation of the tail volume coefficient is given by the following equations

$$C_{VT} = \frac{L_{VT} S_{VT}}{b_w S_w} \quad (73)$$

$$C_{HT} = \frac{L_{HT} S_{HT}}{b_w S_w} \quad (74)$$

Table 35 Tail Geometry Sizing

Vertical Tail		Horizontal Tail	
Vertical Tail area	0.06 m2	Horizontal Tail area	0.14 m2
Vertical Tail Span	0.27 m	Horizontal Tail Span	0.84 m
Aspect Ratio Vertical Tail	5	Aspect Ratio Horizontal Tail	5
Taper Ratio, λ	0,8	Taper Ratio, λ	0,7
Tail Volume	0.02	Tail Volume	0.5185
Length from Vertical tail AC to CG	0.9 m	Length from Horizontal tail AC to CG	1 m

4.4.9 A.4 Fuselage Sizing

Fuselage is designed to provide adequate space for the internal components of the UAV which are the fuel cell, hydrogen tank, battery, receiver and the servos. The following table summarizes the size of the fuselage. The maximum width is determined by the demands for space for installing the internal components. Since the biggest component is the hydrogen tank with a diameter of 120 mm, the fuselage width must be more than 120 mm wide. In addition, the wing joint to the fuselage should be taken into consideration because it will consume some space inside the fuselage. Hence, the maximum width 180 mm is taken.

Table 36 Fuselage Geometry Sizing

Fuselage Geometry			
l_f	1750	mm	fuselage length
w_f	180	mm	max fuselage width
h_f	180	mm	max fuselage height
lf/df	9.722		

4.4.10 A.5 Airfoil Selection for Wing Airfoil

In this part several airfoils are studied in order find the best one that will suit the needs of the design. The requirements for the airfoil selection are defined in following list of criteria.

Criteria for selection:

1. High efficiency Cl/Cd
2. Ease of manufacturing
3. Low pitching moment
4. Low drag

There are four candidates that are considered close to such criteria: SD7032, SD7062, NACA4415 and Eppler 214. The comparison is shown in Figure 51.

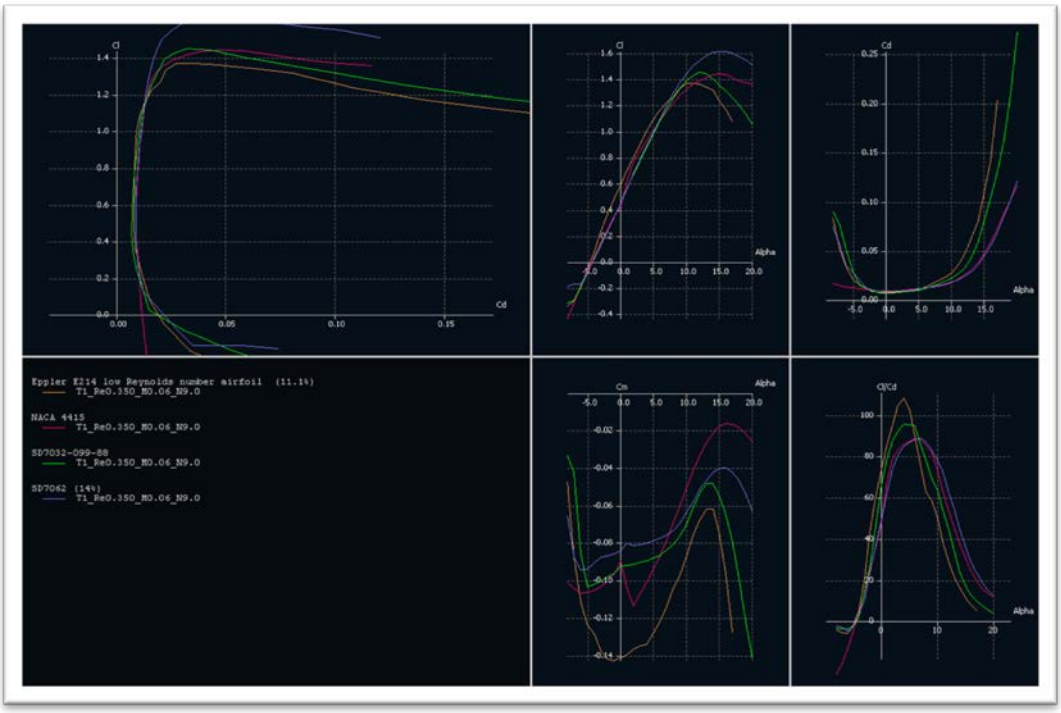

Figure 51 Airfoils Aerodynamics Characteristic Comparison

SD7032 relatively has lower Cl/Cd than E214 but SD7032 has a better pitching moment coefficient. Although the best pitching moment and Cl_{max} is SD7062, the lowest drag is SD7032. Therefore it is more preferable since the power source is very low. Thus, it is decided to use SD7032. Figure 52 shows the 3D model of the UAV.

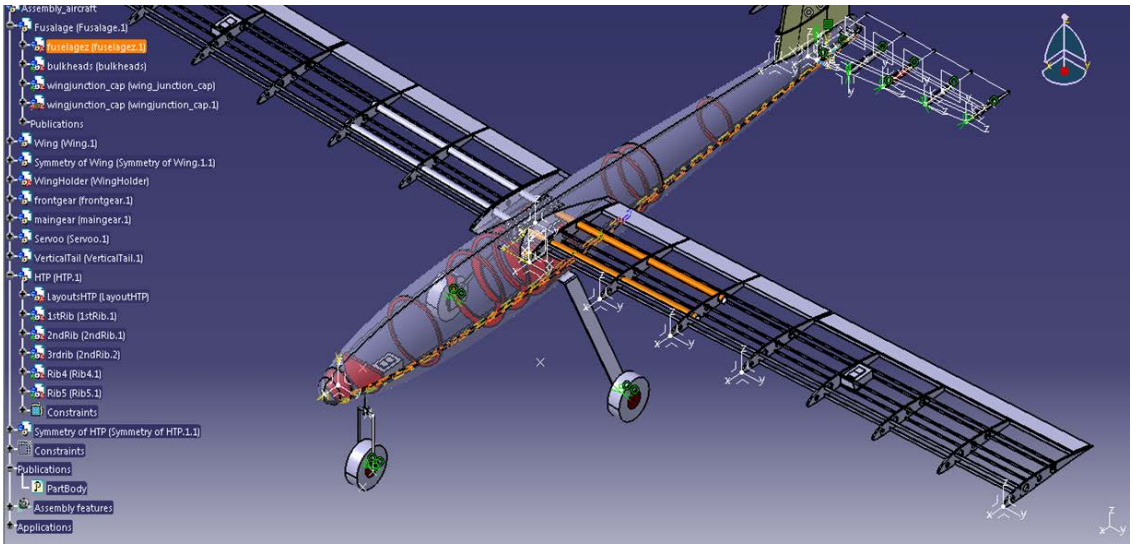

Figure 52 3D CAD Model of the UAV

The UAV is built from composite material (mostly carbon fiber). The reason for choosing this material is because it strong yet lightweight. The fuselage will be made purely from carbon fiber composite. Therefore the mold is being produced by the composite supplier, Premier Composite L.L.C. The mold is depicted in Figure 53 and the final product sample is shown in Figure 55. Figure 54 shows the wing of this UAV manufactured using a carbon fiber sandwiched structure with balsa wood. This sandwich structure is used as the ribs of the wing. The leading edge and trailing edge are purely balsa wood. It has two spar tubes made of carbon fiber as well. The wing is wrapped with a mylar film acting as the skin for the wing.

Figure 53 The Mold for Fuselage Part Built by Premier Composite

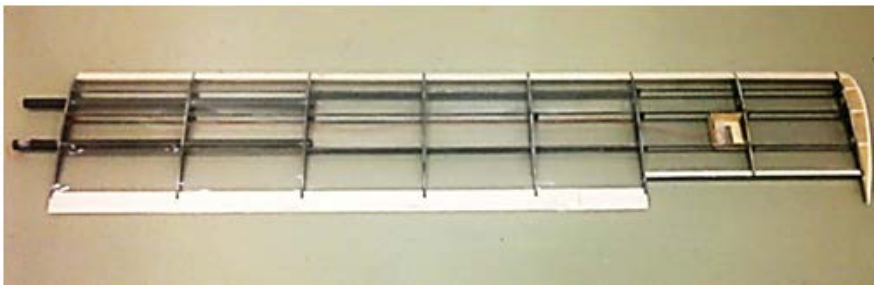

Figure 54 The Wing Made from Carbon Fiber Composite and Balsa Wood

Figure 55 Fuselage Final Product Sample and The Assembly Jigs

B. Load Cell Calibration

Figure 56 shows the calibration result of the load cell reading against the discrete load that was conducted. The load cell has a sensitivity of 1.008 mV/N and is rated for a 100 N tension load.

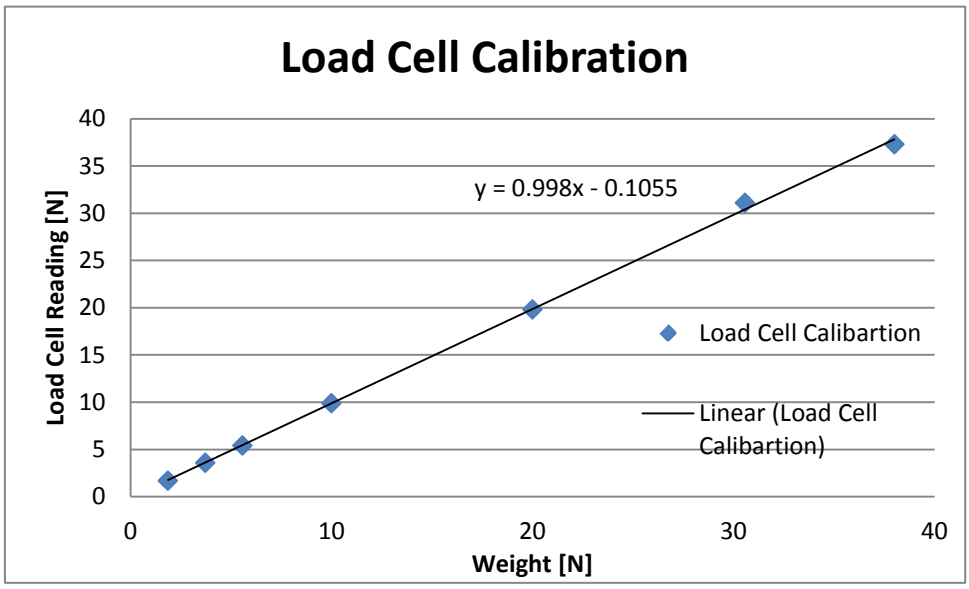

Figure 56 Load Cell Calibration Chart

C. Differential pressure sensor

From the test of the sensor it was found that the sensor voltage output was giving more than its ideal value when there was no airflow. This means there was no pressure difference (see Figure 57). Therefore, a test was conducted in order to calculate the offset.

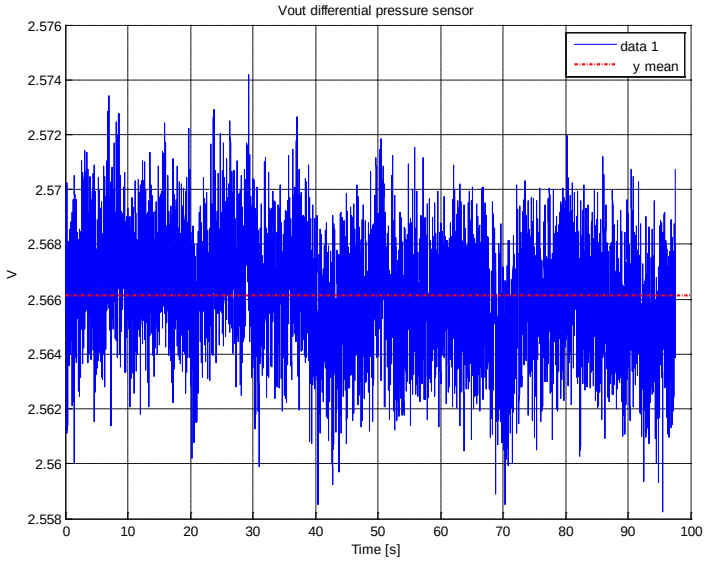

Figure 57 Output Voltage from Differential Pressure Sensor at 0 kPa

The ideal voltage value for the zero differential pressure is 2.5 volts (see Figure 58). Therefore, the recorded voltage is then subtracted by 2.5 volts to find the average value of the difference. This is then used as the offset value to obtain the actual transfer function line as shown in Figure 58.

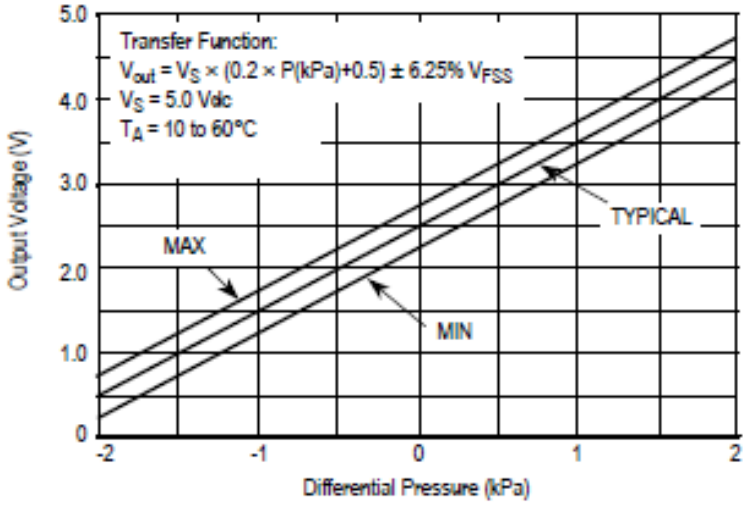

Figure 58 Input Output Mapping of MPXV7002 Sensor [27]

8. Vita

Muhammad Zulkifli was born on July 26th, 1985 in Bandung, Indonesia. He earned a Bachelor of Engineering Degree in Aeronautics and Astronautics from Bandung Institute of Technology in 2009. In 2010, Mr. Zulkifli joined the Masters program in Mechatronics Engineering at the American University of Sharjah, UAE. His field of interest ranges from aerodynamics, propulsion systems, mechatronics systems, CAD modeling, CFD and FEA. Currently he is joining a multinational engineering consulting company GEXCON Indonesia in March 2013.